BNL-224152-2023-JAAM

GRP-COCA-10

Atomic Structural Origin of the High Methanol Selectivity over In2O3-Metal Interfaces: Metal-Support Interactions and the Formation of a InOx Overlayer in Ru/In2O3 Catalysts during CO2 Hydrogenation

N. Rui, J. A. Rodriguez

To be published in "ACS Catalysis"

March 2023

Chemistry Department

Brookhaven National Laboratory

U.S. Department of Energy

USDOE Office of Science (SC), Basic Energy Sciences (BES) (SC-22)

DISCLAIMER

Atomic structural origin of the high methanol selectivity over In_2O_3-metal interfaces: Metal-support interactions and the formation of a InO_x overlayer in Ru/In_2O_3 catalysts during CO_2 hydrogenation

Ning Rui[1,ł], Xuelong Wang[1,ł], Kaixi Deng[2], Jorge Moncada[1], Rina Rosales[2], Feng Zhang[3], Wenqian Xu[4], Iradwikanari Waluyo[5], Adrian Hunt[5], Eli Stavitski[5], Sanjaya D. Senanayake[1], Ping Liu[1,2*], José A. Rodriguez[1,2,3,] *

[1] Chemistry Division, Brookhaven National Laboratory, Upton, NY 11973, USA

[2] Department of Chemistry, Stony Brook University, Stony Brook, NY 11794, USA

[3] Materials Science and Chemical Engineering Department, Stony Brook University, Stony Brook, NY 11794, USA

[4] X-ray Science Division, Advanced Photon Source, Argonne National Laboratory, Lemont, IL 60439, USA

[5] National Synchrotron Light Source II, Brookhaven National Laboratory, Upton, New York 11973, USA

[ł] N. Rui and X. Wang contributed in equal terms to this research.

* Corresponding Authors: pingliu3@bnl.gov; rodrigez@bnl.gov

Abstract: CO_2 hydrogenation to methanol is of great environmental and economic interest due to its potential to reduce carbon emissions and to produce valuable chemicals in one single reaction. Compared with unmodified traditional $Cu/ZnO/Al_2O_3$ catalyst, an indium oxide (In_2O_3)-based catalyst can double the methanol selectivity from 30-50% to 60-100%. It is worth noting that over catalysts involving various active metals dispersed on indium oxide (M/In_2O_3, M=Pd, Ni, Au, etc), although the methanol yield is boosted, the selectivity stays similar to that of plain In_2O_3 despite the distinct chemical properties of the added metals. To investigate the phenomena behind this behavior, here we used RuO_2/In_2O_3 as a test catalyst. The results of ambient-pressure photoelectron spectroscopy, in-situ X-ray absorption fine structure, and time-resolved X-ray diffraction indicate that the structure of the RuO_2/In_2O_3 catalyst is highly dynamic in the presence of a reactive environment. Specifically, under CO_2 hydrogenation conditions, Ru clusters facilitate the reduction of In_2O_3 to generate In_2O_{3-x} aggregates, which encapsulate the Ru systems in a migration driven by thermodynamics. In this way, the Ru^0 sites for CH_4 production are blocked, while creating RuO_x-In_2O_{3-x} interfacial sites with tunable metal-oxide interactions for selective methanol production. In an inverse oxide/metal configuration, the indium oxide has properties not seen in its bulk phase that are useful for the binding and conversion of CO_2. This work reveals the dynamic nature of In_2O_3-based catalysts, providing insights for a rational design of materials for the selective synthesis of methanol.

Keywords: CO_2 hydrogenation; methanol synthesis; hydrogen; ruthenium; indium oxide

1. Introduction

Carbon dioxide (CO_2) is a well-known greenhouse gas that wreaks havoc on the climate and seas globally.[1,2] In recent years, the conversion and utilization of CO_2 have been extensively studied to lower the carbon footprint.[3] The transformation of CO_2 to methanol (CH_3OH) is a desired solution because the alcohol can be utilized as a fuel and prospective energy carrier directly, or as a key precursor in the synthesis of other chemicals.[3] The most common catalyst for methanol synthesis is a $Cu/ZnO/Al_2O_3$ composite.[4,5] A study of high-resolution transmission electron microscopy (HR-TEM) has shown that the active phase of industrial $Cu/ZnO/Al_2O_3$ catalysts consists of a layer of graphitic ZnO on top of the copper.[6] The reconstruction of the catalyst into an inverse oxide/metal configuration is the product of a strong metal-support interaction.[6] This oxide migration is similar to that observed for the Pt/TiO_2 system by Tauster *et al* in their landmark study that pointed to the effects of metal-support interactions in catalysis.[7] New catalytic materials are being tested since the commercial $Cu/ZnO/Al_2O_3$ catalyst without any modification suffers from low methanol selectivity (usually between 30 to 50%).[8]

Recently, indium oxide (In_2O_3) has emerged as an attractive active catalyst due to its high selectivity towards the direct $CO_2 \rightarrow$ methanol conversion (60 to 100%) and high stability.[8] Oxygen vacancies are identified as active sites for activating and hydrogenating CO_2 to methanol selectively, while the competitive reverse water-gas shift reaction (RWGS) forming CO is energetically hindered.[9,10] Since hydrogen activation is the most demanding step in the mechanism, supported metals have been investigated to alleviate this drawback and boost the catalyst activity of indium oxide.[11] Among many metals investigated, palladium has been identified as the most active component to produce methanol with a yield of 0.96 $g_{MeOH}\ h^{-1}\ g_{cat}^{-1}$.[12,13] Other than Pd,[12,13] platinum (Pt),[14,15] iridium (Ir),[16] rhodium (Rh),[17] ruthenium (Ru),[18] nickel (Ni),[19,20] cobalt (Co),[21]

silver (Ag),[22] and gold (Au)[23,24] have been added to reach an improved methanol yield. When combined with a regular support (e.g., CeO_2 and zeolites), Pd and Pt are usually used for CO_2 hydrogenation to $CO/CH_4/CH_3OH$,[25] while Ir and Rh are to produce CO/CH_4.[26] Bulk-like Ru, Ni, and Co are well-known methanation catalysts with a selectivity close to 100%.[27] Ag and Au are seldomly used for the CO_2 hydrogenation reaction since their lack of affinity toward hydrogen due to filled d-bands.[22,23] Overall, these metals show distinct properties and catalytic performance for CO_2 hydrogenation reaction when combined with regular supports.[25–27] However, when any one of these metals was deposited on an In_2O_3 surface, the CH_3OH productivity was boosted.[12–24] The selectivity to CH_3OH of these supported catalysts is usually over 70% with less than 30% of CO formation.[12–24] No CH_4 is produced even when Ru, Ni, or Co is used.[18–21] In general, the selectivity of supported In_2O_3-based catalysts is similar to that of plain In_2O_3. For example, Liu *et al* showed that nano-sized metal particles (Pd, Pt, Rh, Ru, Ir, Ni, Co, Ag, Au) on In_2O_3 enabled a promotional effect with methanol selectivity around 60 – 80%.[13–24] In addition, Pérez-Ramírez *et al* employed an unified synthetic protocol to prepare M/In_2O_3 catalyst (M = Pd, Pt, Rh, Ru, Ir, Ni, Co, Ag, Au), with a metal loading of 0.5 wt.%. The results found that although CO_2 conversion was significantly different, the methanol selectivity was always between 60 % - 90% with CO as the only byproduct.[11] Thus, there is an important phenomenon that has not been addressed and explained: Why is the selectivity similar independence of the supported metal's chemical properties? In this work, we tried to answer this fundamental question from structural and electronic viewpoints. To date, a fundamental understanding of the dynamic structure of In_2O_3-metal interfaces under reaction conditions and their influence on the surface reactivity is generally lacking.

Here, we used ruthenium supported indium oxide (Ru/In_2O_3) as a test catalyst to investigate the dynamic nature of the active sites. Ru was chosen because it is one of the most affected metals by interactions with indium oxide: Isolated Ru is an active and selective methanation catalyst,[27] but when it is combined with In_2O_3, the selectivity is steered to produce methanol instead of methane.[18] In-situ characterizations and calculations based on density functional theory (DFT) were combined to reveal the secret of this large change in selectivity under CO_2 hydrogenation reaction conditions: Ru^0 nanoparticles were encapsulated by RuO_x and In_2O_{3-x} overlayers. The active RuO_x-In_2O_{3-x} interfacial sites block the Ru^0 sites necessary for CH_4 formation, while boosting the catalytic performance towards CH_3OH synthesis by promoting the activation of CO_2 and hydrogenation of formaldehyde. Wherein, the tunable In_2O_3-Ru interaction was found to play an essential role. This work reveals the dynamic structure of the In_2O_3-based catalyst in response to a reactive environment, a phenomenon that matches the behavior seen for Cu/ZnO,[6] and can be extrapolated to similar catalysts used in C1 chemistry.

2. Methods

2.1 Preparation of the catalysts

The indium oxide support was prepared by decomposition of $In(OH)_3$, a process which is described in detail elsewhere.[23] The introduction of Ru onto the In_2O_3 was carried out by a deposition-precipitation method, using a Ruthenium (III) nitrosyl nitrate as the precursor and urea as the precipitation agent. Typically, 0.013 g of Ruthenium (III) nitrosyl nitrate was dissolved in 50 mL of distilled water under stirring for half an hour. After that, 0.495 g of as-prepared In_2O_3 and 0.297 g of urea were added into the solution and stirred for another 1 hour. Then the suspension was heated up to 80 °C and aged for 3 hours. The sample was collected by vacuum filtering, then

transferred to a freeze dryer overnight to remove any moisture. The obtained catalysts will be referred to as Ru/In_2O_3 with a Ru loading of 1 wt%.

2.2 Characterization of the catalysts

Transmission Electron Microscopy (TEM). The TEM measurements were performed on a JEOL JEM-2100F system. The sample was dispersed in ethanol solution and dropped onto a Cu grid for the observation.

Ambient Pressure X-ray Photoelectron Spectroscopy (AP-XPS). The AP-XPS studies were conducted at the AP-PES end station of the IOS (23-ID-2) beamline at the National Synchrotron Light Source II (NSLS-II) at Brookhaven National Laboratory (BNL) using a SPECS Phoibos 150 NAP electron energy analyzer. XPS spectra were collected at UHV to ambient pressures (<1 Torr) through the use of a 300 μm aperture cone and differentially pumped analyzer electron optics, which allows collection of electrons at ambient pressure while keeping the analyzer under near UHV. More details about the beamline and end station are described elsewhere.[28] The photon energies employed were as follows: 740 eV (In 3d, In 4d, O1s, and Ru 3d), and 460 eV (In 4d, Ru 3d, and C1s). All binding energy calibrations were conducted by alignment of the spectra to the Fermi level. For the H_2 reduction, samples were exposed to pure H_2 at 800 mTorr. For the CO_2 hydrogenation reaction, samples were exposed to a mixture of H_2 (800 mTorr) and CO_2 (200 mTorr) at 25-300 °C.

X-ray absorption spectroscopy (XAS). XAS measurements were carried out at the 8-ID beamline at the NSLS-II of BNL. The *in-situ* Ru K-edge (22117 eV) and In K-edge (27940 eV) X-ray absorption near edge structure (XANES) spectra and extended X-ray absorption fine structure (EXAFS) spectra were collected using the fluorescence mode in a Clausen cell flow reactor under atmospheric pressure.[29] The catalyst (~2 mg) was loaded in a quartz tube (1.0 mm

OD and 0.9 mm ID), and pure H_2/CO_2 or a gas mixture of 2 ml/min CO_2 and 8 ml/min H_2 was introduced to the system. The sample was heated from room temperature to the desired temperatures with a 10°C/min ramping rate. The energy calibration was done based on a Ru or In foil. Data processing was performed using the IFEFFIT package.[30]

Time Resolved X-ray Diffraction (TR-XRD). The *in-situ* TR-XRD measurement for the Ru/In_2O_3 catalysts under hydrogen reduction and CO_2 hydrogenation conditions were performed with a Clausen cell flow reactor under atmospheric pressure, at beamline 17-BM (λ=0.24141 Å) of the Advanced Photon Source (APS), in Argonne National Laboratory (ANL). The catalyst (~2 mg) was loaded in a quartz tube (1.1 mm OD and 0.9 mm ID), and a gas of 8 ml/min H_2, or 2 ml /min CO_2 + 8 ml/min H_2 was introduced to the system. The sample was heated from room temperature to the desired temperatures with a 10°C/min ramping rate. Two-dimensional XRD images were collected continuously with a Perkin Elmer detector (amorphous Si flat panel) through the measurement processes. GSAS-II was used to calibrate the diffraction patterns and then covert the XRD raw data to obtain diagrams of intensity versus 2θ. The Rietveld refinement was also performed by GSAS-II.[31]

Pulse CO chemisorption was performed using an Altamira AMI-300 iP catalyst characterization system to measure the CO uptake of reduced metallic Ru sites.

Hydrogen temperature programed reduction (H_2-TPR). The reduction behaviors of samples were analyzed by a hydrogen temperature-programmed reduction (H_2-TPR) method using a chemisorption analyzer (Micromeritics Autochem II 2920). The measurements were carried out in a U-type quartz tube loaded with 100 mg samples. The sample was firstly pretreated at 200 °C for 1 h under the flowing helium. The sample was then cooled down to -50 °C by liquid nitrogen.

After switching to a flow of 10% H_2 in N_2, the sample was ramped to 500 °C with a rate of 10 °C/ min. The H_2 consumption was detected by a thermal conductivity detector (TCD).

2.3 Hydrogen activation ability detection by WO_3

In a typical run, a mixture containing 0.2 g of WO_3, and 0.002 g of catalyst was placed in a quartz reaction tube and held in place with silica wool. Then the tube was placed in an oven with the temperature ranging from RT to 300 °C. Then the hydrogen (molar ratio H_2:N_2 = 3:97) was allowed to flow through the tube at a rate of 50 mL/min. After 30 min, the color of the powder samples was recorded.

2.4 Catalytic activity tests

The CO_2 hydrogenation reaction was carried out under a 5 MPa pressure. The catalyst (100 mg) was loaded in a fixed-bed reactor. A gas mixture of hydrogen, carbon dioxide, and nitrogen at a molar ratio of H_2:CO_2:N_2=76:19:5 was used during the reaction. The reaction was performed with a gas hourly space velocity (GHSV) of 21,000 $cm^3/(g_{cat}\cdot h)$ and a temperature range from 200 to 300 °C. Products were analyzed using an online gas chromatograph (Agilent 7890), equipped with TCD and FID detectors. CO_2 conversion (X_{CO_2}), CH_3OH selectivity (S_{CH_3OH}) and CH_3OH formation rate were calculated as follows:

$$X_{CO_2} = \frac{F_{CO_2,\,in} - F_{CO_2,\,out}}{F_{CO_2,in}} \times 100\%$$

$$S_{CH_3OH} = \frac{F_{CH_3OH,\,out}}{F_{CO_2,\,in} - F_{CO_2,\,out}} \times 100\%$$

$$CH_3OH\ \text{formation rate} = \frac{X_{CO_2} \times S_{CH_3OH} \times F_{CO_2,in}}{W}$$

where F and W are the molar flow rate and the sample weight, respectively.

2.5 Calculations using Density Functional Theory (DFT)

The density functional theory (DFT) calculations in this work were performed with the Vienna Ab Initio Simulation Package (VASP)[32–35] using the projector-augmented wave (PAW) approach[36]. The generalized gradient approximation (GGA) type exchange-correlation functional in the parameterization of Perdew, Burke, and Ernzerhof (PBE) was adopted.[37] The energy cutoff for the basis set of wave functions was set to be 500 eV. The *k*-mesh was generated at least denser than the density of one point per 0.03 $Å^{-3}$ with Gamma point included to ensure the accuracy of calculation results. For the relaxation of model structures, the forces felt by each atom were well converged smaller than 0.03 eV/Å.

For In_2O_3 catalyst, the surface model was built based on the bulk In_2O_3 structure in $Ia\bar{3}$ space group with optimized lattice parameters a=b=c=10.3476Å. Following previous theoretical studies[10,38,39], the active (110) surface was cut from the bulk in a $(\sqrt{2} \times 1)$ supercell with dimensions a=14.6337Å and b=10.3476Å. To simulate the inverse active structure, for In_2O_3 catalyst supported on Ru surface, supporting Ru (001) surface was cut from optimized hcp Ru bulk structure (a=b=2.7133Å, c=4.2846Å) in a $(3\sqrt{3} \times 4)$ supercell with dimensions a=14.0987Å and b=10.8532Å. A row of In_2O_3 with the repetition unit In_4O_6 was put on the Ru (001) surface to simulate the In_2O_3 catalyst cluster since the In_4O_6 monomer is the smallest unit of In_2O_3 (110) surface and it contains all the active sites for CO_2 reduction reaction, as reported by previous studies.[10,38,39] For both catalyst models, a 20Å vacuum layer was placed over the surface to eliminate the interactions between periodic slab images. For In_2O_3 model catalyst, 4 layers of In_2O_3 was used with bottom 2 layer fixed during optimization. For Ru supporting In_2O_3 model catalyst, 3 layers of Ru was used with bottom 1 layer fixed during optimization. The part of Ru (001) surface not covered by In_2O_3 cluster was terminated by oxygen sitting at hcp hollow site.

The oxygen vacancy was generated by removing one surface oxygen from the perfect model catalysts and its formation energy was referenced to CO_2, H_2, and H_2O. The relative energies of all adsorbates and intermediates were referenced to perfect catalyst surface as:

$$E_f = E(intermidiate/surface) + x \cdot E(H_2O) - y \cdot E(H_2) - E(CO_2) - E(surface).$$

where E_f is the formation energy (chemical potential) of surface adsorbates, $E(intermidiate/surface)$ is the total energy of slab model with adsorbates, $E(H_2O)/E(H_2)/E(CO_2)$ is the total energy of $H_2O/H_2/CO_2$ single molecule, and $E(surface)$ is the total energy of bare surface slab model.

3 Results and Discussion

3.1 TEM studies on the morphology of Ru/In_2O_3 catalysts

The morphology of the as-prepared and reduced RuO_2/In_2O_3 catalyst was characterized using high-resolution electron transmission microscopy (HR-TEM). For the as-prepared systems, the TEM images showed mainly surfaces of In_2O_3 and no clear features that could be attributed to Ru or RuO_2 were observed (Figure S1) due to a low loading of the admetal (1 wt%) and its high dispersion. In a set of studies, the RuO_2/In_2O_3 sample was reduced at 200 °C before loading it into the TEM. The corresponding images are shown in Figure 1(a-c), confirming that crystalline In_2O_3 particles were present in the reduced catalysts. The Fourier transform pattern with Miller indices for the cubic In_2O_3 in Figure 1(a) features (222), (440) and (400) facets.[40] No Ru is observed in the HR-TEM images of Figure 1(a) and (b). Elemental mapping was used to find out

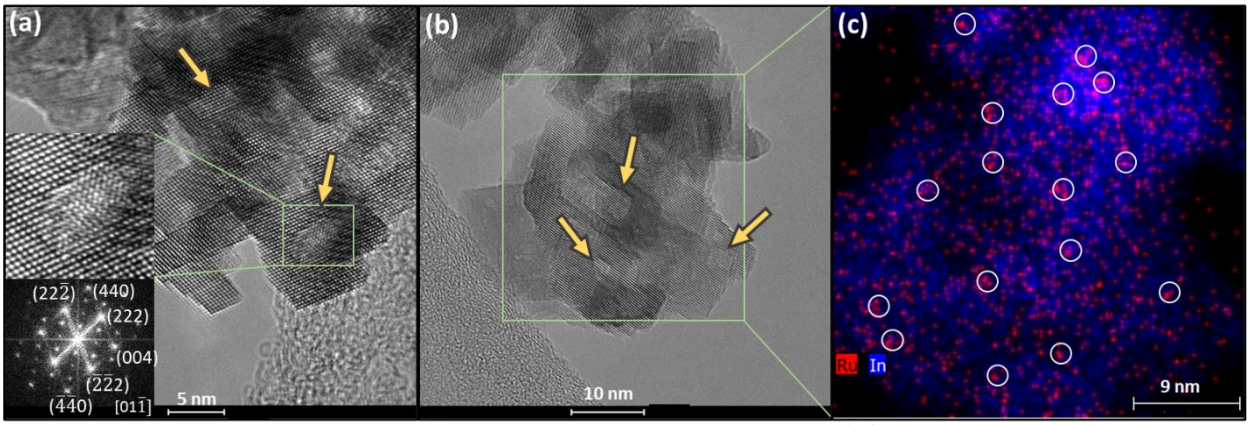

Figure 1 (a, b) HR-TEM images of reduced Ru/In_2O_3 catalyst, (c) EDX elemental mapping of selected areas of a Ru/In_2O_3 catalyst. The arrows point out the existence of oxygen vacancies. Insertion of (a): top, enlarged image of oxygen vacancy; bottom; Miller indices assignment of Fast Fourier Transform (FFT) patterns of TEM images. In part (c), the white circles denote small Ru clusters

the distribution of Ru in Figure 1(c), showing that Ru (white circles) was evenly dispersed on the In_2O_3 support forming small nanoparticles (NPs) that now were clearly recognized. In addition, defect sites are labeled with yellow arrows and enlarged in Figure 1(a). These disordered features can be attributed to oxygen vacancies caused by H_2 reduction. Since these features are not present in the sample prior to reduction, Figure S1. The images and data in Figure 1 are consistent with a configuration where very small particles of Ru/RuO_x are partially buried into the indium oxide support or covered by aggregates of In_2O_{3-x}. A configuration that is derived from the experimental and studies described below.

3.2 Identification of the surface structure and its H_2 activation ability

To determine the reactivity of the as-prepared RuO_2/In_2O_3 catalyst towards H_2 activation, H_2-TPR tests were conducted in the temperature range between -50 and 500 °C, as shown in Figure 2(a). At temperatures below 300 °C, the reactivity of plain indium oxide towards H_2 is very

low.[8,9,11] From 25 to 300 °C, our RuO_2/In_2O_3 catalyst consumed much more H_2 than plain In_2O_3, pointing to a higher surface reactivity. Interestingly, a sharp H_2 consumption peak is seen around RT (highlighted in Figure 2a). This can be assigned to the reduction of a RuO_2 in the oxide-oxide interface. Supported RuO_x NPs are usually reduced around 190 °C,[41] The fact that the reducing temperature is lowered to around RT highlights the importance of the interaction between the RuO_2 and In_2O_3 components. Since the amount of ruthenium present in the catalyst was very small, the TPR data indicated that both oxide components in the catalyst were being reduced, which is consistent with results of AP-XPS discussed below.

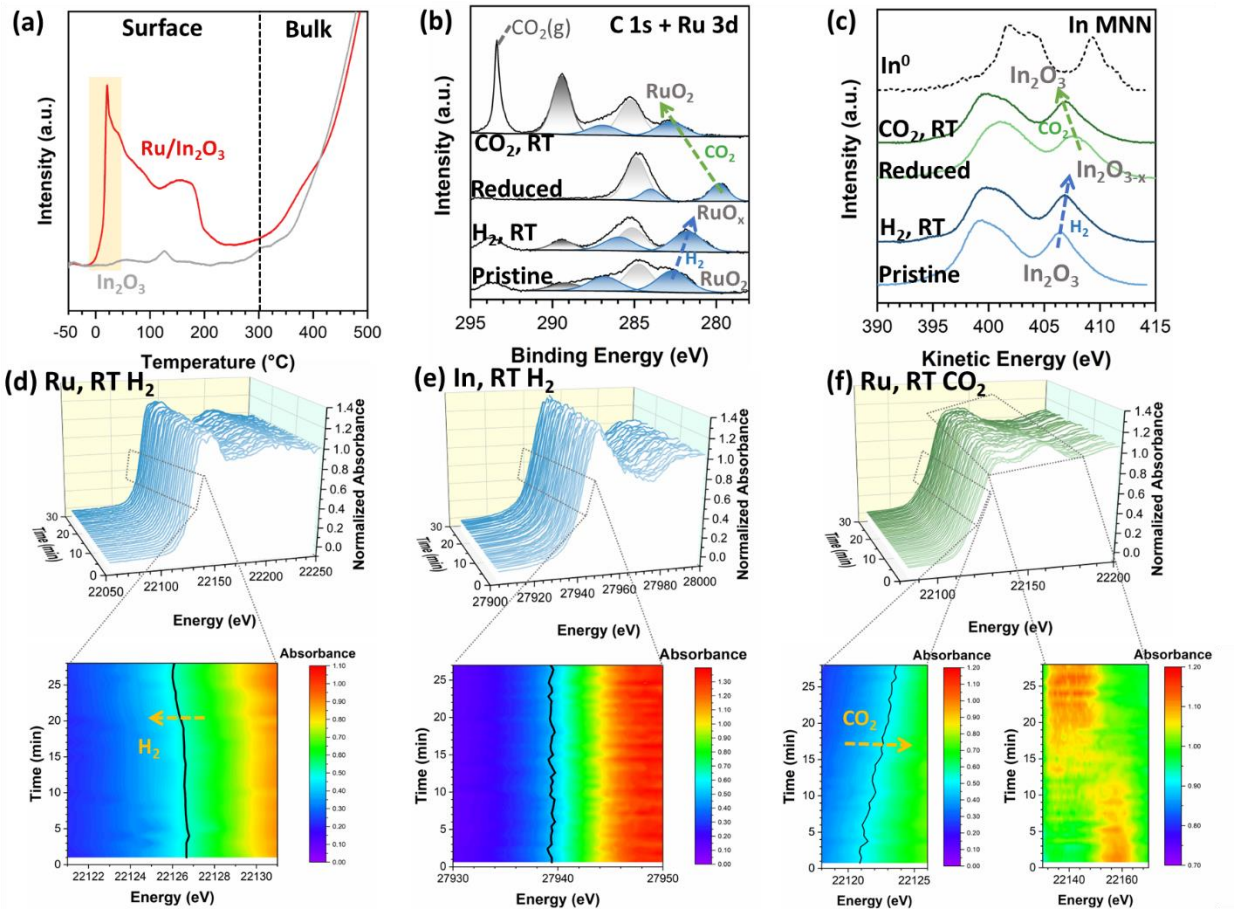

Figure 2. (a) H_2-TPR profile of Ru/In_2O_3 and plain In_2O_3 support from -50 to 500 °C. (b and c) C 1s + Ru 3d and In MNN AP-XPS peaks of a Ru/In_2O_3 catalyst as-prepared and under different gases at room

temperature (RT). From bottom to top: UHV, 750 mTorr of H_2, reduced sample under UHV, and 250 mTorr of CO_2. (d and e) Ru and In K-edge XANES spectra of a Ru/In_2O_3 catalyst under H_2 at room temperature for 30 min; (f) Ru K-edge XANES spectra of a Ru/In_2O_3 catalyst under CO_2 at room temperature for 30 min. The contour maps in the bottom row show the changes of edge energy (black lines) and white line feature over time.

To get more detailed information of the reduction process, ambient pressure X-ray photoelectron spectroscopy (AP-XPS), which is surface sensitive, and in-situ X-ray absorption near edge structure (XANES) spectra, which is a bulk technique, were collected at RT with H_2 flowing over the sample. Due to the pressure limitations in the operation of AP-XPS instruments,[28] the photoemission and Auger spectra were collected at a maximum gas pressure of 750 mTorr. In the Ru 3d XPS spectra in Figure 2(b), the binding energy (B.E.) of the Ru $3d_{5/2}$ peak shifted from 282.5 to 281.7 eV after interacting with H_2 (B.E. of Ru^0 is 279.7 eV).[42] It can thus be suggested that RuO_2 was partially reduced to RuO_x. For the In MNN features in Figure 2(c), the kinetic energy (K.E.) also shifted from 333.6 to 333.1 eV (the K.E. of In^0 is 330.7 eV), indicating a partial reduction to In_2O_{3-x} with the creation of oxygen vacancies.[23] The reduction is related to the active interfacial oxygen atoms, which can be removed by H_2 easily even at RT (Figure S2).[43] H_2 dissociation is also evidenced by the emergence of an OH* peak in Figure S2 ($H_2 + 2O_{lattice} \rightarrow 2OH^*$). For the in-situ XANES data, collected under an atmospheric flow of 10% H_2 in N_2, the oxidation state changes are shown in contour plots, with the adsorption edges marked by black lines. The position of the edge was determined by the half-height energy position of the XANES spectra.[44] In Figure 2(d), the shift of the Ru K edge energy from 22126.7 eV to 22126.0 eV indicates that bulk RuO_2 is reduced by H_2 to RuO_x, as seen in the AP-XPS data of Figure 2b. However, for the In K edge in Figure 2(e), the edge energy stays around 27939.5 eV, showing no bulk reduction. Overall, at room temperature, the catalyst is active for H_2 activation: RuO_2 is

reduced in both the surface and bulk, while In_2O_3 is only reduced in its surface. Neither the AP-XPS data in Figure 2c nor the XANES data in Figure 2e are consistent with the formation of a Ru-In alloy.

Next, we tracked the evolution of the surface structure during the H_2 activation process with synchrotron-based high-resolution AP-XPS. At 300 °C, the binding energy of the Ru $3d_{5/2}$ peak was 279.7 eV, indicating that Ru is in a metallic state (Figure S3).[42] We calculated the In/Ru ratio, which shows the relative concentration of In and Ru on the catalyst's surface, following the equation:

$$\text{In/Ru ratio} = \text{A(In 4d)/A(Ru 3d)}$$

Where A(In 4d) stands for the peak area of the In 4d features and A(Ru 3d) stands for the area of the Ru 3d features. For an easier comparison, and to take into account differences in the cross sections of the In 4d and Ru 3d core levels, the peak areas were normalized to those of the pristine sample. To vary the probing depth, two photon energies were used to collect In 4d and Ru 3d data: 460 eV and 740 eV. According to the universal curve, data collected with 460 eV is more surface sensitive than at 740 eV (with a difference of 3-5 Å in the probing depth of the electrons).[45] The results are summarized in Figure 3(a). Clearly, once the temperature reaches 200 °C, the In/Ru ratio increase in both photon energies. Especially, the increase is more predominately with a 460 eV photon energy, which is more surface sensitive.[45] This suggests that the In is concentrated on the surface other than in the bulk. In other words, In_2O_{3-x} and Ru reverse places and form an oxide/metal structure where the surface of the metallic Ru^0 is decorated by In_2O_{3-x} aggregates.

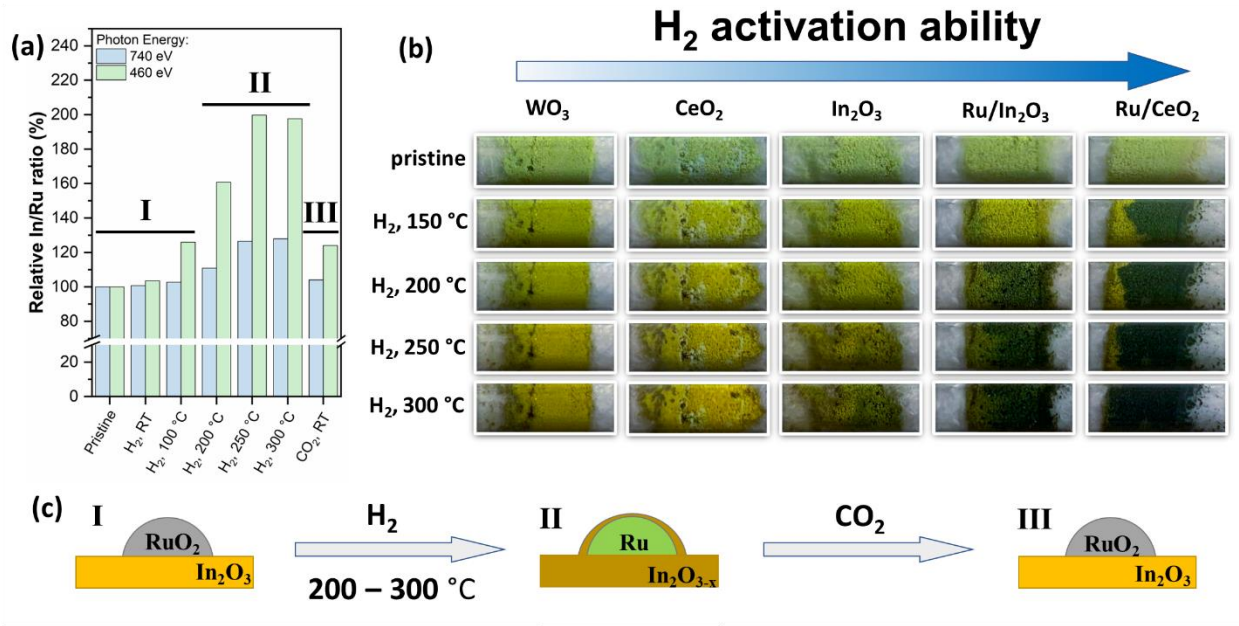

Figure 3. (a) Relative In(4d)/Ru(3d) ratio calculated from AP-XPS data. In each experiment, the In 4d and Ru 3d peak areas were normalized to those of the pristine sample; (b) photographs of samples made with 1 g of WO_3 mixed with 0.01 g of various catalysts after treatment with H_2 at various temperatures for 30 min; (c) a scheme for the evolution of the catalyst structure as a function of reactant.

To further verify the existence of this unique encapsuled structure, its CO uptake was determined. In this composite system, metallic Ru chemisorbs CO strongly, while RuO_2 and In_2O_3 show little adsorption.[46] After H_2 reduction at 300 °C, the CO uptake is 223.1 μmol g^{-1} for the Ru/CeO_2 catalyst, while it decreased dramatically to 0 μmol g^{-1} for Ru/In_2O_3 as shown in Table 1. This indicates that Ru/CeO_2 has highly dispersed Ru^0 sites on the surface, but no bare Ru^0 is exposed in Ru/In_2O_3, confirming our hypothesis proposed on the basis of the AP-XPS results. It is worth noting that the migration of In_2O_{3-x} onto the Ru surface took place at 200 ~ 300 °C, which is lower than for most conventional reducible supports.[26,47-49] For example, the migration temperature of CeO_2 and TiO_2 is typically higher than 500 °C,[48,49] although in some cases

formation of an oxide overlayer has been seen at 250-300 ^{o}C.[49] It is important to point out that an inverse ZnO_x/Cu active configuration has been found with TEM for Cu/ZnO/Al_2O_3 catalysts used for the synthesis of methanol from CO_2 hydrogenation.[6] As seen in this study, reduction by hydrogen induce the migration of the oxide substrate to the surface of the supported metal.

Table 1. CO adsorption amount (μmol g^{-1}) of Ru/CeO_2 and Ru/In_2O_3 catalysts calculated from CO pulse chemisorption experiments

Samples	**CO uptake (μmol g^{-1})**	
	200 °C, H_2	300 °C, H_2
Ru/CeO_2	174.5	223.1
Ru/In_2O_3	46.9	0.0

After reduction, the In_2O_{3-x} overlayers cover the metallic Ru surface. There remains an important question: Will this unique structure still be active for H_2 dissociation? To answer this question, we mixed various catalysts with WO_3 and recorded their colors under different conditions, Figure 3(b). This is because if the catalyst can activate H_2 molecules, the spilled-over hydrogen adatoms migrate and readily react with the yellow WO_3 to form dark blue H_xWO_3.[50] Therefore, the darker the color, the greater the H_2 activation capacity. As seen in the photographs in Figure 3(b), the pure WO_3 and CeO_2 became slightly yellowish due to the dehydration after heating, showing no H_2 dissociation ability. Ru/In_2O_3 is darker than plain In_2O_3 but lighter than Ru/CeO_2 with hydrogen treatment, indicating that hydrogen dissociation ability rises in the order Ru/CeO_2 > Ru/In_2O_3 > In_2O_3. These results suggest that this unique encapsulated structure can still dissociate H_2 effectively. This is also in line with the observed catalytic performance observed below where the CO_2 conversion increases in the same sequence: Ru/CeO_2 > Ru/In_2O_3 > In_2O_3.

To determine the reversibility of the decoration layer, we treated the reduced sample with pure CO_2 at room temperature. As shown by the corresponding AP-XPS and XANES data in Figure 2, CO_2 was activated and re-oxidized both Ru^0 and In_2O_{3-x}. In Figure 3(a), the In/Ru ratio is also restored mostly to a pristine state, confirming that the initial reduction process is reversible. Overall, the structure of the Ru/In_2O_3 catalyst is sensitive to the reactants, as summarized in the cartoon of Figure 3(c).

3.3 Driving force for Ru encapsulation in RuOx/ In_2O_{3-x}: Theoretical studies

To understand the driving forces for the observed encapsulation of Ru^0 by RuO_x and In_2O_{3-x}, the phenomenon was investigated using DFT. For CeO_2-based systems, the encapsulation of metal particles by CeO_x is usually reported to occur above 500 °C.[49] In this study, the encapsulation of Ru NPs was observed to occur already at 200-300 °C due to a very strong interaction with the In_2O_3 support. The facilitated encapsulation may be a consequence of the mobility of surface In atoms. Using DFT, we calculated the energy cost to move an In cation from $In_2O_{3-x}(110)$ to $RuO_x/Ru(001)$ as a function of the content of O vacancies (O_v) in the indium oxide substrate. The results in Table 2 show that the In migration from $In_2O_{3-x}(110)$ to a $RuO_x/Ru(001)$ surface is initially very endothermic, but then switches to an exothermic process when the concentration

Table 2. Energy cost to move an In cation from a $In_2O_{3-x}(110)$ substrate with different O_v concentrations to a $RuO_x/Ru(001)$ surface. (In, purple; O, red; Ru, light grey)

Surface O_v concentration	ΔE (eV/In atom)
8.33%	+4.566
16.67%	+1.750
25%	+0.956
33.33%	-0.298

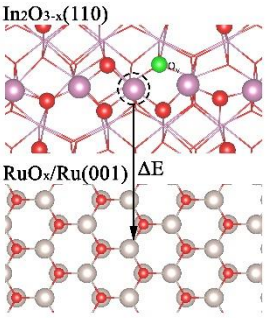

of oxygen vacancies (Ov) increases by reaction with hydrogen: The more reduced the In_2O_{3-x}(110) surface, the less energy is required for the In displacement. When the reduction level of the In_2O_3(110) substrate is high enough (i.e. a lost over 33% of the surface oxygen atoms), an In cation is not stable on In_2O_{3-x}(110), and thermodynamically prefers to relocate on RuO_x/Ru(001). Such reduction of In_2O_3 can be easily reached by depositing Ru (see Figure 2a), which is accompanied with electron transfer from Ru to In_2O_3. Given that, under a reducing atmosphere, the produced In_2O_{3-x} can be well stabilized by a direct interaction with Ru sites in the vicinity of RuO_x particles, via a In_2O_{3-x}-RuO_x/Ru configuration, which confirms the reaction-driven structural dynamics of Ru/In_2O_3 proposed experimentally (Figure 3c).

3.4 **Catalytic performance of the reduced RuO_2/In_2O_3 catalysts**

The AP-XPS and XANES results shown in Figure 2 indicate that the reduced RuO_2/In_2O_3 systems can activate CO_2 and H_2 at room temperature. In a set of studies, the CO_2 hydrogenation reaction was investigated over these catalysts. In_2O_3, Ru/Al_2O_3 and Ru/CeO_2 catalysts were also tested for the purpose of comparison. The results are illustrated in Figures 4(a-c), methanol selectivity and yield, and S4, CO_2 conversion. In all our catalytic tests, Ru/Al_2O_3 and Ru/CeO_2 were very active for the production of CH_4 with a selectivity larger than 70%, independently of the conversion of CO_2 and reaction temperature {Figure 2(a) and Figure S4}. This demonstrates that Ru, when dispersed on a regular support, is an effective methanation catalyst. However, when Ru NPs are combined with the In_2O_3 support, no methane was detected across all the investigated

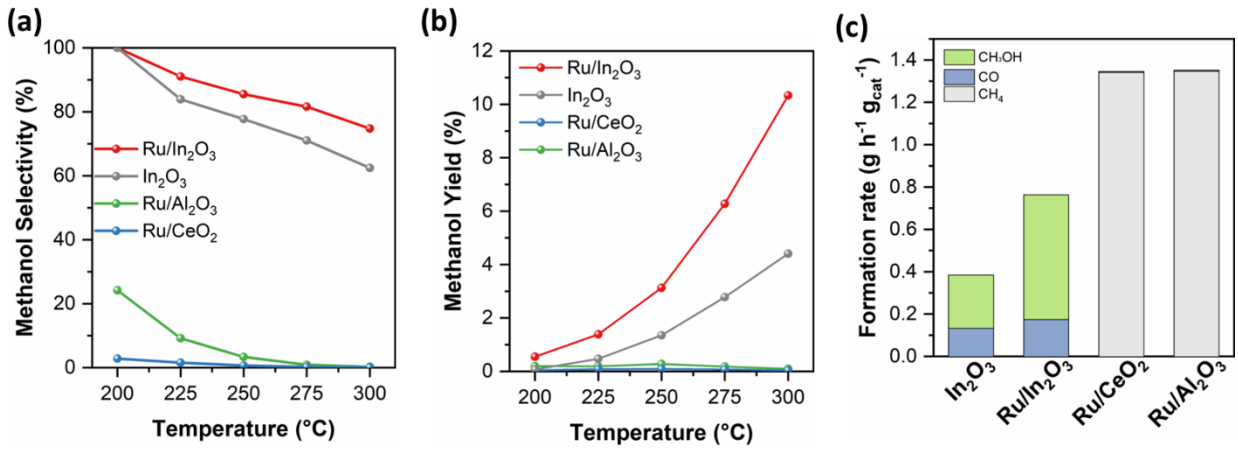

Figure 4 (a) Methanol selectivity and (b) yield over plain In_2O_3 and Ru-based catalysts at different temperatures. The ruthenium was dispersed on indium oxide, ceria and alumina. (c) The product distribution in terms of formation rate over In_2O_3 and various Ru-based catalysts at 300 °C

reaction conditions with methanol and CO as the only products seen. In Figure S4, the CO_2 conversion for all the tested catalysts at 225 °C is below 10%, but the performances of In_2O_3 and Ru/In_2O_3 are unique for methanol production. The introduction of Ru improves the methanol selectivity relative to pure In_2O_3 and doubles the yield, as shown in Figure 4(a) and (b). For example, at 300 °C, the selectivity is 74.7% and the methanol formation rate is 0.59 g_{MeOH} h^{-1} g_{cat}^{-1} over the Ru/In_2O_3 catalyst, while it is only 62.4% and 0.25 g_{MeOH} h^{-1} g_{cat}^{-1} for plain In_2O_3, respectively. This demonstrates that In_2O_3 does alter the catalytic nature of Ru, steering it into an efficient methanol producer instead of a regular methanation catalyst. This dramatic shift in catalytic performance suggests that Ru is probably participating in the reaction in an unconventional manner or covered by aggregates of In_2O_{3-x} (Figure 3c).

3.5 Configuration of the active catalyst under reaction conditions

In this section, we will discuss whether the unique encapsulated structure seen in Figure 3(c) is feasible under real reaction conditions and how it affects the reactivity. Ru K-edge XANES and EXAFS spectra were collected to follow the short-range bonding environment of Ru/CeO_2 and Ru/In_2O_3 catalysts, as shown in the top panels of Figure 5. Figure 5(a) compares the Ru K-edge XANES spectra for a Ru foil, RuO_2/In_2O_3, Ru/CeO_2, and Ru/In_2O_3 catalysts under reaction conditions. The onset of the Ru K-edge XANES spectra is denoted as feature I. Under reaction condition, the absorption edge of the Ru/CeO_2 catalyst is exactly the same of the metallic Ru foil, while the edge for Ru/In_2O_3 shows a shift to higher energy relative to the Ru foil, indicating the presence of a RuO_x species. In the XANES region, the spectra of Ru/CeO_2 aligns very well with the Ru foil. In contrast for Ru/In_2O_3, it is similar to the one for RuO_2 in region II, while in region III, it resembles the Ru foil. The broad plateau within region II corresponds to contributions from transitions from 1s to 5p states, confirming the existence of RuO_x.[51] Feature III is dominated by the multiple scattering of emitted photoelectrons colliding into heavy elements at the neighboring shells, being a direct evidence for metallic Ru^0.[51] Overall, Ru in Ru/CeO_2 is pure metallic, while Ru in Ru/In_2O_3 is a mixture of RuO_x and metallic Ru.

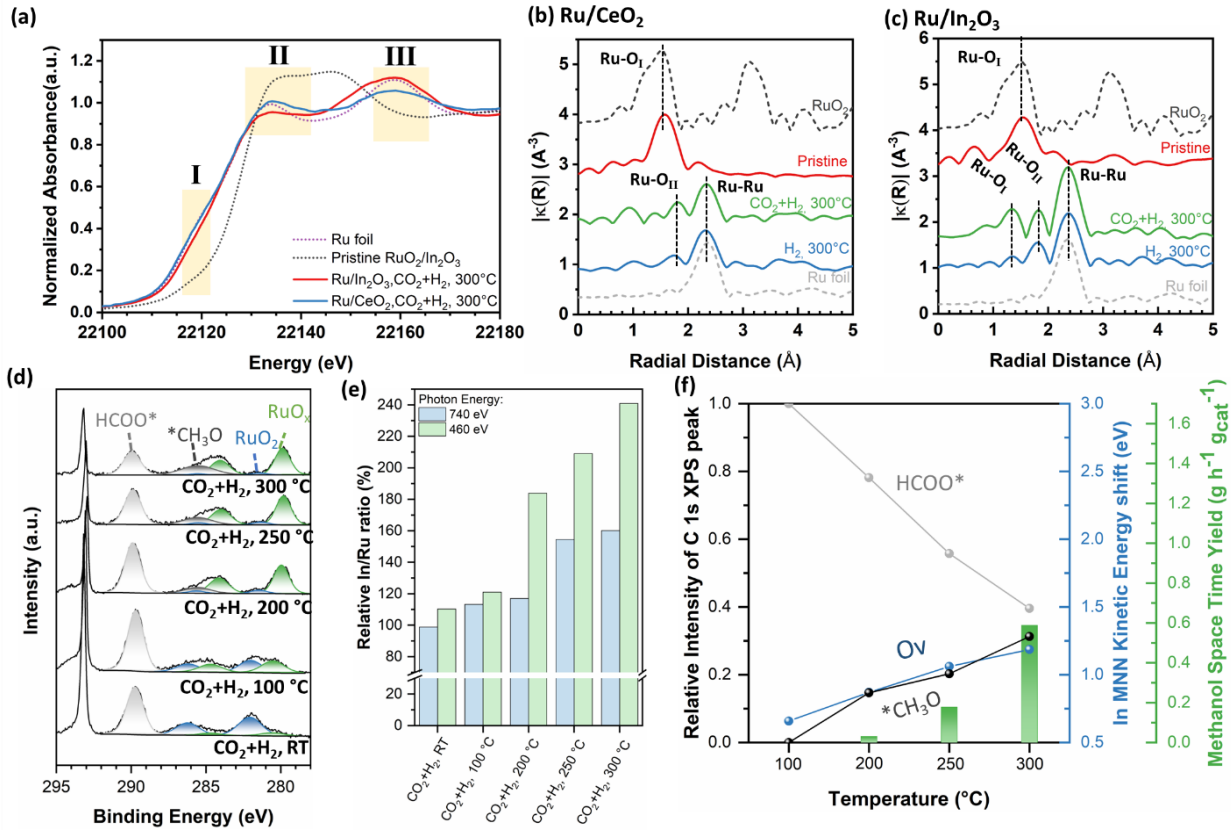

Figure 5. (a) In-situ Ru K-edge XANES spectra and Fourier transformed R-space EXAFS data of (b) Ru/CeO_2 and (c) Ru/In_2O_3 catalysts under various conditions. (d) C 1s + Ru 3d AP-XPS features of a Ru/In_2O_3 catalyst under 250 mTorr CO_2 + 750 mTorr H_2 at various temperatures; (e) Relative In/Ru ratio calculated from the AP-XPS data; (f) the variation of methanol yield, surface intermediate concentration, and concentration of oxygen vacancies as a function of the temperature (the variation in the concentration of oxygen vacancies is determined by the In MNN peak shift in AP-XPS spectra);

To obtain the coordination environment of the Ru atoms, a Fourier transformation was performed to get the R-space EXAFS data as shown in Figure 5(b) and (c). For pristine Ru/CeO_2 and Ru/In_2O_3 samples, we found features very similar to those of the RuO_2 standard and only first-shell coordination with O ($Ru\text{-}O_I$) were observed. The absence of a Ru-Ru bond indicates high overlayer dispersion for both samples. For the Ru/CeO_2 catalyst after reduction at 300 °C, in Figure 5(b), a Ru-Ru (~2.63Å) bond appears, indicating the formation of metallic Ru.[52] A feature for a

regular R-O_{II} bond is seen at ~ 1.9 Å, which can be assigned to a Ru bond with interfacial O from the CeO_2 support.[52] The interfacial Ru-O_{II} bonds are further enhanced under a $CO_2 + H_2$ mixture, suggesting the importance of ruthenium sites during the reaction. For the Ru/In_2O_3 catalyst after reduction at 300 °C in Figure 5(c), in addition to a metallic Ru-Ru bond (~2.63Å), the Ru-O_{II} peak is also seen with higher intensity compared to that in the Ru/CeO_2 catalyst. Similarly, this bonding can be assigned to Ru that binds with interfacial O from In_2O_{3-x} overlayers. Significant changes can be seen when comparing the ruthenium EXAFS features under plain H_2 and under a CO_2/H_2 reaction mixture. Another weak Ru-O_I bond emerges, which is slightly shorter than regular Ru-O_I bonds in RuO_2. This can be assigned to Ru bound with oxygen atoms produced by the dissociation of CO_2 on the surface, with a bond shortened due to the nano dimensions of the particles.[53] If CO_2 is introduced ($CO_2 + H_2$), the Ru-O_I bond intensifies strongly, suggesting that under reaction condition, there is some RuO_x species that co-exist with metallic Ru. This conclusion agrees with the in-situ XANES results discussed above and the results of AP-XPS.

Time resolved XRD (TR-XRD) characterization was conducted to probe the structure of Ru/In_2O_3 catalyst in the long-range as shown in Figure 6. All the diffraction peaks are originating from crystalline cubic In_2O_3.[23] The absence of a Ru diffraction peak indicates the presence of well dispersed Ru as seen in Figure 1c. For the sample under H_2 (Figure 6a), a noticeable diffraction peak related to In^0 emerged when cooling down to room temperature (enlarged in Figure S5a).[54] Interestingly, under CO_2+H_2 reaction conditions, no such peaks were observed (Figure 6b and S5b). This result clearly indicates that CO_2 can prevent the overreduction of In_2O_{3-x} to In^0. This is consistent with the results of AP-XPS and XANES where no reduction of indium to metallic In^0 or a Ru-In alloy was observed under CO_2 hydrogenation conditions. Rietveld refinement was

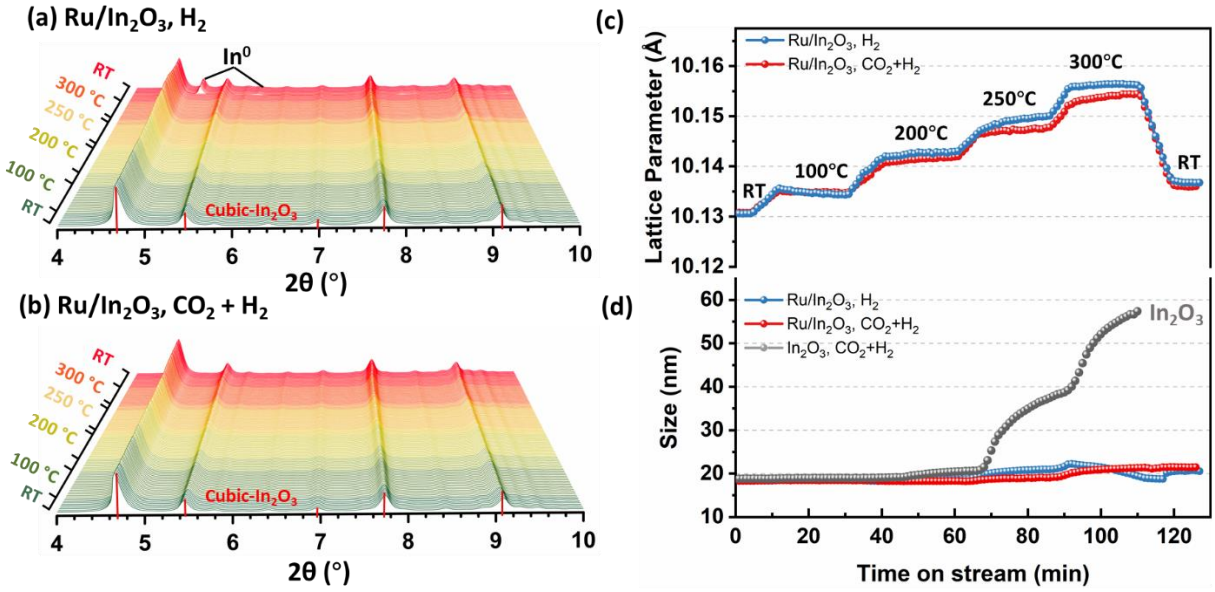

Figure 6. TR-XRD patterns of Ru/In_2O_3 catalyst under (a) H_2 reduction and (b) $CO_2 + H_2$ reaction conditions; Rietveld refinement results of (c) lattice parameter of Ru/In_2O_3 catalyst under H_2 or CO_2+H_2 conditions; (d) In_2O_3 particle sizes of plain In_2O_3 and Ru/In_2O_3 catalyst under H_2 or CO_2+H_2 conditions.

performed to the diffraction patterns in Figure 6(b) to get structural information about the cubic In_2O_3 lattice parameters and particle size, as shown in Figure 6 (c) and (d), respectively. With the formation of oxygen vacancies, the system expands, showing a larger lattice parameter.[23] Clearly, the lattice expansion under reaction condition was less than that produced by pure hydrogenation. The results are consistent with the fact that CO_2 can prevent In_2O_3 from over-reduction, as well emphasizing the significance of In_2O_{3-x} for activating CO_2.[23] An analysis of the particle size of Ru/In_2O_3 catalyst revealed that it was constant at ~20 nm under various conditions. However, for plain In_2O_3, the particle size increased dramatically above 200 °C due to the amorphization of In_2O_3.[54] It is therefore likely that the Ru NPs can prevent the In_2O_3 from sintering under reaction conditions, contributing to the high stability of the catalytic material.

3.6 Reaction intermediates on RuO_x-In_2O_{3-x}/Ru: AP-XPS studies

In Figure 2(b)-(c) are shown the AP-XPS results for the adsorption of CO_2 on the reduced RuO_2/In_2O_3 catalyst at 300 K. The dissociation of CO_2 leads to reoxidation of ruthenium and indium and a strong peak for a formate (HCOO*) and/or carbonate (CO_3*) species is seen near 290 eV. The AP-XPS results collected under a CO_2/H_2 atmosphere are summarized in Figures 5(d) and S6. In Figure 5(d), there are clear changes in the signal for Ru/RuOx when the sample is exposed to a reaction mixture of CO_2/H_2 at difference temperatures (100-300 ^oC). The B.E. of RuO_x under reaction conditions at 300 °C is 280.0 eV, 0.3 eV higher than that in pure H_2 (Figure S3). This shift indicate that Ru is in a RuO_x state on the surface due to re-oxidation by CO_2.[52] Furthermore, formate or carbonate (~289.5 eV)[55] and methoxy (*CH_3O, ~286.0 eV)[55] species were detected as the reaction intermediates, which strongly confirms previous DRIFTS and DFT studies.[10,56] The relative stability of these species could be affected by changes in the structural configuration of the catalyst.[57-63] Formate, methoxy and carboxyl species are frequently cited as intermediates in the conversion of CO_2 to CH_3OH.[10,56,57,64] In general, the rates for the transformation of these intermediates depend on the temperature and on the structure/composition of the catalyst.[10,56,57,64] In some situations, these species are plain spectators.[10,56,57,64]

The In/Ru ratio is displayed in Figure 5(e), showing the same trend as that seen in pure H_2 (Figure 3a). These findings provide additional support for an encapsulated structure under CO_2 + H_2 reaction conditions, with some RuO_x co-existing on the surface. To illustrate the relationship between the density of oxygen vacancies, the concentration of reaction intermediates, and the methanol production rate as a function of temperature, existing correlations were summarized in Figure 5(f). Clearly, at higher temperatures, the density of oxygen vacancies increases, while formate species are probably transforming into methoxy, and the methanol production rate

increases accordingly. Based on these facts, we conclude that oxygen vacancies play a vital role in the reaction, and formate and methoxy are two essential intermediates that take part in the chemical transformation of CO_2, in agreement with the finding of previous studies.[9,10]

3.7 Reaction mechanism on RuO_x-In_2O_{3-x}/Ru: Theoretical studies

The exact structural geometry of the RuO_x-In_2O_{3-x}/Ru interface is not known. The in-situ data of AP-XPS and XANES point to the reaction of ruthenium and indium oxides with CO_2 and H_2. On the basis of the experimental studies described above, models were constructed to compare in qualitative terms the hydrogenation of CO_2 on In_2O_3(110), RuO_x/Ru(001) and In_2O_3/RuO_x/Ru(001) surfaces. Figures 7(a) and 7(b) show structural configurations for a In_2O_3(110) surface and a film of RuO_x on Ru(001), making sure that both Ru and In_2O_3 are exposed to reactant molecules of CO_2 and H_2 and participate in the transformation of CO_2 to CH_3OH. In Figure 7(a), one can select a repetitive unit area or ribbon of In_2O_3(110) surface where for each repeating unit, In_4O_6 motit, four indium cations (In_n, n= 1,4) are bound with six O anions (O_n, n= 1,6). This ribbon of In_2O_3 was deposited on oxygen-covered Ru(001) or a RuO_x/Ru(001) substrate, Figure 7(c). In our model, the In_2O_3 ribbon was anchored on the RuO_x support via the O atom at the Ru site and In at the O site (see side view in Figure 7c). Such inverse structure is denoted here as In_2O_3/RuO_x/Ru(001). The In_2O_3(110) surface was also included in our study for comparison, since

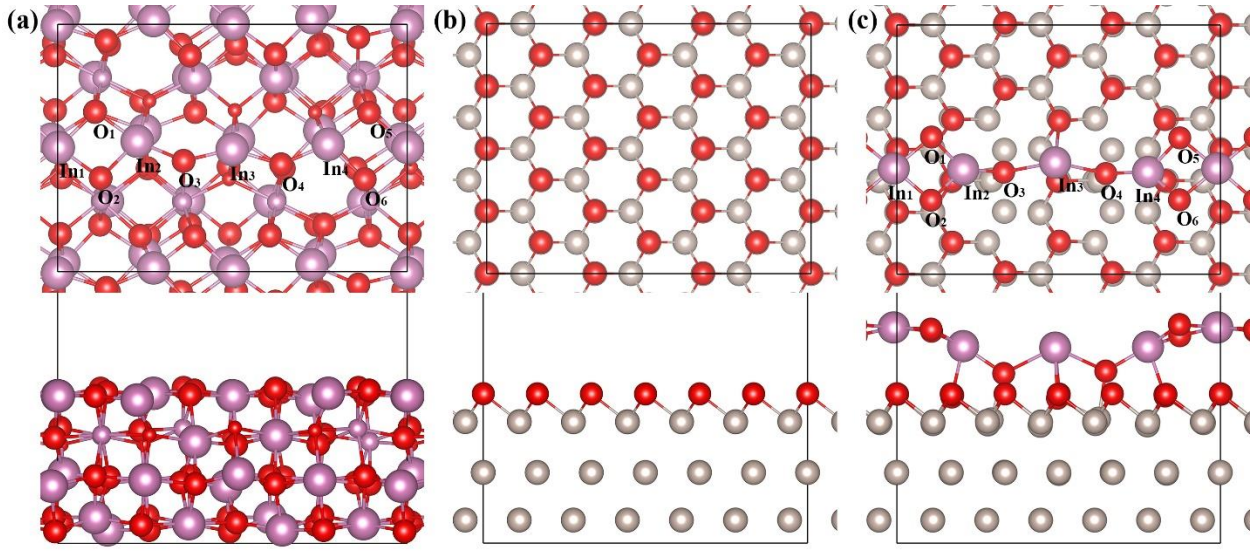

Figure 7 Top and side views of optimized model structures for (a) In_2O_3(110), (b) RuO_x/Ru(001) and (c) In_2O_3/RuO_x/Ru(001) surfaces (In, purple; O, red; Ru, light gray. For clear viewing purposes, atoms under surface layer will be shown as backbones in the following figures)

it is known as an active catalyst for CO_2 hydrogenation to CH_3OH .[10,38]

The In_2O_3 rows supported on RuO_x/Ru(001) and In_2O_3(110) display a similar structure. Both consist of tetragon-like In_1-O_1-O_2-In_2, chain-like In_2-O_3-In_3-O_4 and tetragon-like In_4-O_5-O_6-In_1 motifs in one supercell (Figure 7(a)). Differently, there are two types of oxygen on In_2O_3 supported by RuO_x/Ru(001), which are exposed and available for the reaction: one is the interfacial oxygen, which interacts with both In and surface Ru at the In_2O_{3-x}-Ru(001) interface ($O_{3,4}$); the other is the surface oxygen, which solely binds with In and locates on the top of In_2O_3 ($O_{1,2,5,6}$, Figure 7(c)). While only one type is seen for In_2O_3(110), which only interacts with In centers with a coordination number of three. In addition, according to the calculated partial density of states (pDOS) (Figure S7(a)), there is a charge transfer from Ru to In for In_2O_3/RuO_x/Ru(001), which leads to the reduction of In^{3+}. That is, although the In cation of In_2O_3/RuO_x/Ru(001) should adopt

3+ oxidation state, it is reduced due to the electron transfer from the Ru support. In the case of In_2O_3(110), In likely remains as 3+.

Key intermediates and elementary steps involved in CO_2 hydrogenation were investigated on In_2O_3(110) and $In_2O_3/RuO_x/Ru$(001) to shed light on the effect that the Ru support made on the catalyst activity and CH_3OH production selectivity. A series of previous works by Ge and co-workers reported that O_V are prone to emerge on In_2O_3(110) surfaces at reducing conditions with H_2 or CO.[10,38] Indeed, among the six O sites in a single In_4O_6 motif, Figure 7(a), the O_v sites created by removing O_3 or O_4 are found to be the most active for CO_2 adsorption and further hydrogenation, which largely determines the conversion efficiency of CO_2 gas. Furthermore, Ge and coworkers also discovered that the rate limiting step for methanol production on a In_2O_3(110) surface is the hydrogenation of monodentate $*CH_2O$ to $*CH_3O$ at the O_V site, which is related to the $*CH_2O$ being stabilized by co-adsorbed *H at neighboring In and O sites (mono-$*CH_2O$+$*H_{In}$+$*H_O$).[10,38] Therefore, instead of studying the whole reaction pathway, we only focused on the key steps in the current DFT calculations including the O_V formation, CO_2 adsorption, and the conversion of mono-$*CH_2O$+$*H_{In}$+$*H_O$ as showing in the following discussion. Our main objective is a qualitative comparison of the surface chemistry on In_2O_3(110) and $In_2O_3/RuO_x/Ru$(001).

The origin of the promoted CH_3OH production/selectivity by formation of a Ru-In_2O_3 interface is associated with a tunable metal-oxide interaction. It can be strong enough to enhance the reduction of In^{3+} cations and facilitate O_v generation and CO_2 adsorption. The strong interaction of In_2O_3 with Ru is demonstrated by the significant hybridization between Ru and the interfacial O atom of In_2O_3, Figures 8(b) and S7(a). Consequently, the state of the surface $In^{\delta+}$ cations involved in CO_2 hydrogenation upshifts toward the Fermi level when moving from In_2O_3(110) to $In_2O_3/RuO_x/Ru$(001). This is also accompanied with the reduced ionic nature of In-O interaction.

As a result, the In-O bonds are weakened, which facilitates the generation of O_v. Upon adsorption at the O_v site, Figure S7(b), the $*CO_2$ is stabilized in the form of carbonyl $CO_2^{\delta-}$-like species on both systems. However, the electron density at the O_v site is relatively localized on In_2O_3 (110), which limits the binding to $*CO_2$; by comparison the stronger $*CO_2$ binding on $In_2O_3/RuO_x/Ru(001)$ by 0.56 eV is associated with the Ru support-promoted delocalization of electron density and thus stabilization of $*CO_2$, Figure S7(b).

On the other hand, the Ru-In_2O_3 interaction can be weakened by the hydroxylation of In_2O_3 under CO_2 hydrogenation conditions. This is the case seen for mono-$*CH_2O$+$*H_{In}$+$*H_O$ (Figure 8b). The dissociation of H_2 can lead to the hydroxylation of interfacial O_4 ($*H_O$) and In_4 ($*H_{In}$). As a result, both Ru-O_4 and In_4-O of RuO_x bonds are broken, Figure 8(b), which is demonstrated by the significant profile changes for the pDOS of In and O of In_2O_3, Figure S7(c). More importantly, it results in the suppression of the charge transfer from Ru to mono-$*CH_2O$ at the In_3 site, Figure S7(c). Therefore, mono-$*CH_2O$ is destabilized at the In_4 site of the In_2O_3-$RuO_x/Ru(001)$ interface more significantly by 0.31 eV than that of In_2O_3 (110), where the surface O atoms are stable and the corresponding atomic/electronic structures are less affected by hydroxylation, Figure S7(c). The hydrogenation of mono-$*CH_2O$ by $*H_{In}$ to produce $*CH_3O$ partially removes the hydroxylation of In_2O_3. Consequently, the In_4 re-interacts with O atom of RuO_x, and a strengthened binding to $*CH_3O$ on $In_2O_3/RuO_x/Ru(001)$ as compared to that of In_2O_3 (110) is observed, as seen for the case of $*CO_2$. Yet, the magnitude of bond strengthening for $*CH_3O$ (0.15 eV) is much less than that of $*CO_2$, which again reflects a suppression by hydroxylation, Figure S7(d). Given that, the interaction between In_2O_3 and the Ru(001) support can be essential to tune the binding to the reaction intermediates involved in CO_2 hydrogenation and thus the catalytic activity/selectivity.

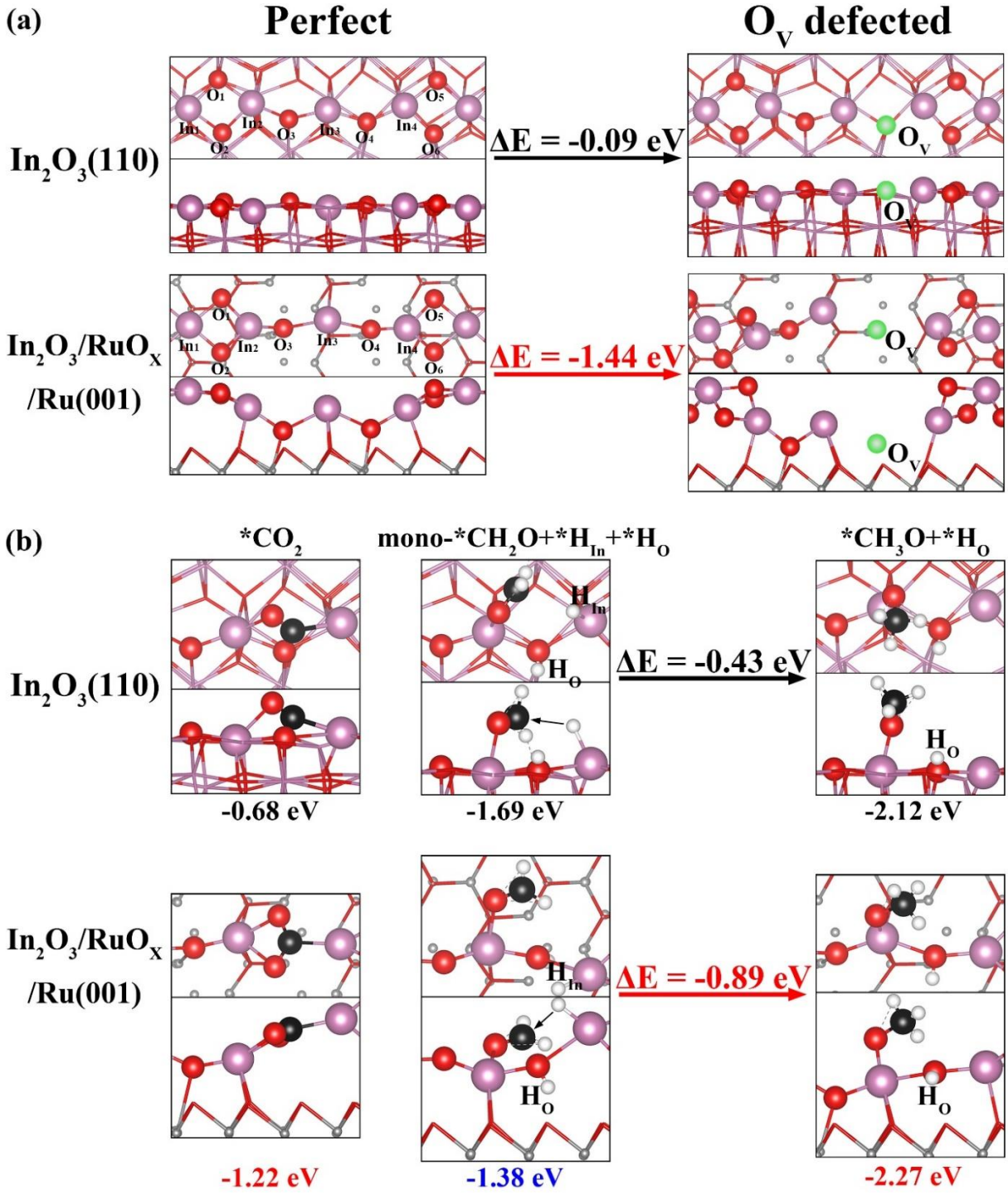

Figure 8 (a) Optimized structures for In_2O_3(110) and In_2O_3/RuO_x/Ru(001) surfaces with and without oxygen vacancies (O_v); (b) Optimized structures for some key intermediates: *CO_2, mono-

CH_2O+H_{In}+*H_O, and *CH_3O+*H_O on In_2O_3(110) and In_2O_3/RuO_x/Ru(001) surfaces. (P: perfect surface; D: surface with O_v: In, purple; O, red; Ru, small light gray; C, black; H, white)

The experimental data shown in Figure 2 indicate that the high reactivity of In_2O_3/RuO_x towards H_2 is essential to form the unique active sites and thus display exceptional chemical properties of this catalyst. In the case of pure In_2O_3, a limited reactivity towards H_2 leads to a low conversion of CO_2.[8–10] The decrease of the positive charge on the $In^{\delta+}$ cations seen in the case of In_2O_3/RuO_x/Ru(001) favors the generation of O_v. For example, the energy necessary to remove an O_4 atom is decreased from -0.09 eV/O_v on the In_2O_3(110) surface (consistent with the result reported in ref.[10]) to -1.44 eV/O_v on In_2O_3/RuO_x/Ru(001), Figure 8(a). This suggests a higher concentration of active O_v sites at the In_2O_3-Ru(001) interface than on the In_2O_3(110) surface under same condition. Furthermore, the generated O_v site on In_2O_3/RuO_x/Ru(001) is more active than that on In_2O_3(110), being able to provide a stronger binding to CO_2 (binding energy: -0.68 eV vs. -1.22 eV) by accommodating one of the oxygen atoms of the molecule at the O_v site, to heal the defect-rich surface, while the remaining O atom interacts with neighboring In atoms (Figure 8b). The strengthened CO_2 binding can promote the coverage of adsorbed *CO_2 species on In_2O_3 when this oxide is supported over RuO_x/Ru(001). This is in line with our experimental results by CO_2-TPD as shown in Figure S8. Besides, it also likely promotes the CO_2 conversion rate as shown previously.[13]

To address the effect on CH_3OH selectivity, the reaction energy for converting mono-*CH_2O+*H_{In}+*H_O to*CH_3O was calculated . On In_2O_3(110) surface this step releases an energy of 0.43eV in agreement with the previous study.[10] While it is increased to 0.89eV on In_2O_3/RuO_x/Ru(001) . The increased exothermicity can be attributed to destabilized mono-*CH_2O and stabilized *CH_3O when going from In_2O_3(110) to In_2O_3/RuO_x/Ru(001), which helps shift the

equilibrium toward the formation of *CH_3O and thus CH_3OH. In short, with the formation of In_2O_3-RuO_x/Ru(001) interfaces the reactive O_v sites are more easily formed by H_2 reduction, the *CO_2 coverage and corresponding activation are promoted, and the rate-limiting step of *CH_2O hydrogenation to *CH_3O becomes more exothermic. In qualitative terms, all three factors ensure an enhancement in methanol productivity/selectivity when going from In_2O_3 to RuO_2/In_2O_3 as observed experimentally (see Figure 4).

3.8 Inverse oxide/metal configurations and CO_2 hydrogenation

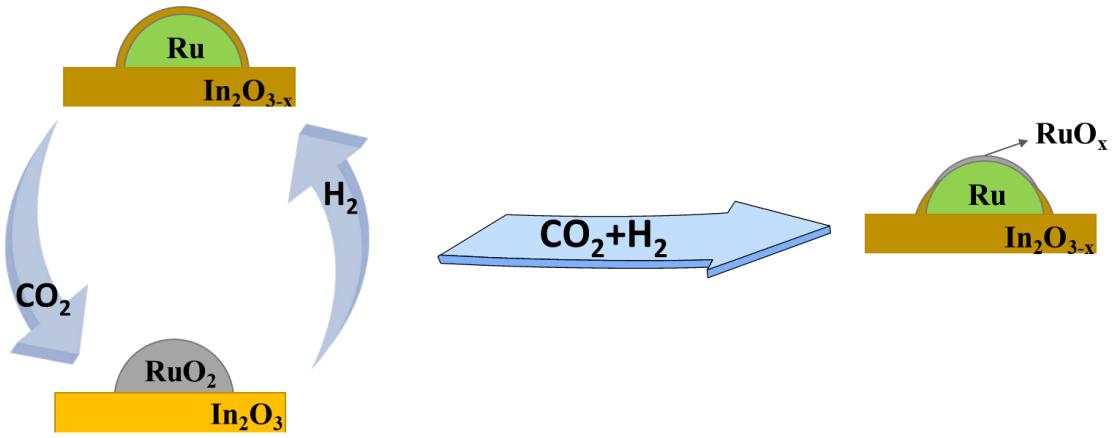

Figure 9. Schematic figure showing the dynamic structure of Ru/In_2O_3 catalyst under various conditions.

On the basis of the experimental and theoretical results analyzed above, it is clear that the atomic structure a RuO_2/In_2O_3 system changes dynamically in response to the reactive environment. Figure 9 summarizes the structural changes. Initially, the pristine catalyst has a configuration with RuO_2 supported on stoichiometric In_2O_3. Under an environment rich in H_2,

RuO_2 and In_2O_3 are reduced to Ru^0 and In_2O_{3-x}, respectively, generating an encapsulated structure containing a metallic Ru core and In_2O_{3-x} overlayers. This unique structure dissociates H_2 more effectively than bulk In_2O_3. With pure CO_2, RuO_x and In_2O_{3-x} will be re-oxidized, and the In_2O_{3-x} overlayer is reversibly removed from the Ru surface. Finally, under CO_2 hydrogenation conditions, the system again adopts a structure with Ru encapsulated. Apart from In_2O_{3-x} overlayers, there is also some RuO_x on the surface. This structure is the key to block metallic Ru^0 from interacting with reactants, thus favoring methanol formation instead of methane with interfacial RuO_x-In_2O_{3-x} sites. Therefore, this unique structure can double the methanol productivity compared with plain In_2O_3. The in-situ studies with AP-XPS and XAFS (Figures 2 and 5) indicate that both components of the catalyst, RuO_x and In_2O_{3-x}, interact with CO_2 and H_2 and are probably involved in the $CO_2 \rightarrow CH_3OH$ conversion, which is consistent with the surface chemistry seen in the DFT calculations (Figure 8). The magnitude of the cooperation between the two oxides is still an open question. The increase in the catalyst activity is small but not negligible at temperatures between 225 and 300 ^oC (Figure S4) and there is a substantial enhancement in the production or methanol (Figure 4).

A comparison of the behavior of many metal-In_2O_3 interfaces (metal= Ru, Co, Rh, Ir, Ni, Pd, Pt, Ag or Au) indicates that all of them have a selectivity towards methanol close 70%,[12–24] as seen during the hydrogenation CO_2 on plain In_2O_3. [9,10] This is independent of the intrinsic nature of the transition metal. Thus, metals that are well-known CO_2 methanation catalysts produce methanol and no methane when bound to indium oxide.[17–20] The surface of these metals also could be covered with by a layer of indium oxide that has special chemical and catalytic properties. Reported data for Ni-In_2O_3 are consistent with a configuration where NiO_y and In_2O_{3-x} aggregates block the access of molecules to plain metallic nickel.[19] More in-situ studies on the structure and morphology of these metal-In_2O_3 interfaces are necessary. An inverse oxide/metal configuration

has been observed in HR-TEM studies for $Cu/ZnO/Al_2O_3$.[6] Indeed, the deposition of nanoparticles of ZnO on copper surfaces produces oxide-metal interfaces with a rich surface chemistry and good activity for the CO_2 → CH_3OH conversion. [5,57] The change in configuration (metal/oxide → oxide/metal) observed for these systems in the presence of H_2 is similar to that seen for the Pt/TiO_2 system[58,59] and highlighted by Tauster as a typical example of metal-support interactions.[7,60,61] These interactions and surface reconstructions can have a negative impact on the catalytic properties of many systems[60,61] but, as discussed above, they can be essential for catalysts used in CO_2 hydrogenation. In an inverse oxide/metal configuration, the oxide usually has properties not seen for bulk oxides,[61–63] and these can be useful in the binding and conversion of CO_2. Key reaction intermediates such as carboxyl, formate and methoxy are easier to transform when present on inverse oxide/metal systems.[5,57,62,65]

4 Conclusions

In this work, we used RuO_2/In_2O_3 as a model system to illustrate how an In_2O_3 support can transform a good CO_2 methanation catalyst into a methanol producer. The results of AP-XPS, in-situ XAFS, and TR-XRD indicate that the structure of a RuO_2/In_2O_3 catalyst is highly dynamic in the presence of a reactive environment. Specifically, under reaction conditions, Ru nanoparticles facilitate the reduction of In_2O_3 to generate In_2O_{3-x} with oxygen vacancies. With a certain concentration of oxygen vacancies, the In_2O_{3-x} will migrate onto the surface of Ru clusters and form encapsulated structures driven by thermodynamics. This mechanism was further confirmed by DFT calculation. The unique encapsulated structure, consisting of Ru^0 nanoparticles decorated with RuO_x and In_2O_{3-x} aggregates on its surface, can inhibit the CH_4 formation by blocking Ru^0

sites, while generating interfacial RuO_x-In_2O_{3-x} sites for the selective hydrogenation of CO_2 to methanol. Compared with plain In_2O_3, the methanol selectivity is improved from 62.4% to 74.7%, and the yield is doubled from 0.25 to 0.59 $g_{MeOH}\ h^{-1}\ g_{cat}^{-1}$. DFT calculation verified that In_2O_{3-x} overlayers are more active than bulk In_2O_3 regarding oxygen vacancy formation, CO_2 activation and its further conversion to methanol, being responsible for the enhanced activity. Wherein, the tunable In_2O_3-Ru interaction was found to play an essential role. This work reveals the dynamic structure of the In_2O_3-based catalyst in response to reactive environment, with potential for extrapolation to other catalysts for C1 chemistry and energy applications.

Declaration of Interests

The authors declare no competing interests.

Associated Content

Supporting Information

The Supporting Information is available free of charge at the ACS web site.

The supporting information includes high-resolution TEM images of the catalyst, AP-XPS spectra collected after exposing the catalyst to H_2, CO_2 and CO_2/H_2 mixtures, in-situ time-resolved XRD patterns for the catalyst recorded under a background of CO_2 and CO_2/H_2, CO_2-TPD traces, and calculated plots for the DOS of the catalyst surface clean and with different adsorbates.

Acknowledgments

The experimental studies carried out at Brookhaven National Laboratory were supported by the US Department of Energy, Chemical Sciences Division (DE-SC0012704). S.D.S. is partially supported by a U.S. Department of Energy Early Career Award. The XAS and AP-XPS experiments of this research used beamlines 8-ID (ISS) and 23-ID-2 (IOS) of the National Synchrotron Light Source II, a U.S. Department of Energy (DOE) Office of Science User Facility operated for the DOE Office of Science by Brookhaven National Laboratory under Contract No. DE-SC0012704. The XRD experiments of this research used beamline 17-BM of the Advanced Photon Source, a U.S. Department of Energy (DOE) Office of Science User Facility operated for the DOE Office of Science by Argonne National Laboratory under Contract No. DE-AC02-06CH11357.

The DFT calculations were performed at Brookhaven National Laboratory and supported by the Division of Chemical Sciences, Geosciences, & Biosciences, Office of Basic Energy Science of the US Department of Energy (DOE) under Contract No. DE-SC0012704. All calculations in this work were conducted using the computational resources at the Center for Functional Nanomaterials, which is a US DOE Office of Science Facility, and the Scientific Data and Computing Center, a component of the Computational Science Initiative, at Brookhaven National Laboratory under Contract No. DE-SC0012704, the Center for Nanoscale Materials, an Office of Science user facility at Argonne National Laboratory, supported by the US DOE, Office of Science, Office of Basic Energy Sciences, under Contract No. DE-AC02-06CH11357, and the National Energy Research Scientific Computing Center (NERSC), which is supported by the Office of Science of the U.S. DOE under Contract No. DE-AC02-05CH11231 using NERSC award BES-ERCAP0019897.

References

(1) Jones, W. D. Carbon Capture and Conversion. *J. Am. Chem. Soc.* **2020**, *142* (11), 4955–4957. https://doi.org/10.1021/jacs.0c02356.

(2) Bushuyev, O. S.; De Luna, P.; Dinh, C. T.; Tao, L.; Saur, G.; van de Lagemaat, J.; Kelley, S. O.; Sargent, E. H. What Should We Make with CO_2 and How Can We Make It? *Joule* **2018**, *2* (5), 825–832. https://doi.org/10.1016/j.joule.2017.09.003.

(3) Tackett, B. M.; Gomez, E.; Chen, J. G. Net Reduction of CO_2 via Its Thermocatalytic and Electrocatalytic Transformation Reactions in Standard and Hybrid Processes. *Nat. Catal.* **2019**, *2* (5), 381–386. https://doi.org/10.1038/s41929-019-0266-y.

(4) Amann, P.; Klötzer, B.; Degerman, D.; Köpfle, N.; Götsch, T.; Lömker, P.; Rameshan, C.; Ploner, K.; Bikaljevic, D.; Wang, H.-Y.; Soldemo, M.; Shipilin, M.; Goodwin, C. M.; Gladh, J.; Halldin Stenlid, J.; Börner, M.; Schlueter, C.; Nilsson, A. The State of Zinc in Methanol Synthesis over a Zn/ZnO/Cu(211) Model Catalyst. *Science* **2022**, *376* (6593), 603–608. https://doi.org/10.1126/science.abj7747.

(5) Kattel, S.; Ramírez, P. J.; Chen, J. G.; Rodriguez, J. A.; Liu, P. Active Sites for CO_2 Hydrogenation to Methanol on Cu/ZnO Catalysts. *Science* **2017**, *355* (6331), 1296–1299. https://doi.org/10.1126/science.aal3573.

(6) Lunkenbein, T.; Schumann, J.; Behrens, M.; Schlögl, R.; Willinger, M. G. Formation of a ZnO Overlayer in Industrial Cu/ZnO/Al_2O_3 Catalysts Induced by Strong Metal–Support Interactions. *Angew. Chem. Int. Ed.* **2015**, *54* (15), 4544–4548. https://doi.org/10.1002/anie.201411581.

(7) Tauster, S. J.; Fung, S. C.; Garten, R. L. Strong Metal-Support Interactions. Group 8 Noble Metals Supported on Titanium Dioxide. *J. Am. Chem. Soc.* **1978**, *100* (1), 170–175. https://doi.org/10.1021/ja00469a029.

(8) Martin, O.; Martín, A. J.; Mondelli, C.; Mitchell, S.; Segawa, T. F.; Hauert, R.; Drouilly, C.; Curulla-Ferré, D.; Pérez-Ramírez, J. Indium Oxide as a Superior Catalyst for Methanol Synthesis by CO_2 Hydrogenation. *Angew. Chem. Int. Ed.* **2016**, *55* (21), 6261–6265. https://doi.org/10.1002/anie.201600943.

(9) Frei, M. S.; Capdevila-Cortada, M.; García-Muelas, R.; Mondelli, C.; López, N.; Stewart, J. A.; Curulla Ferré, D.; Pérez-Ramírez, J. Mechanism and Microkinetics of Methanol Synthesis via CO_2 Hydrogenation on Indium Oxide. *J. Catal.* **2018**, *361*, 313–321. https://doi.org/10.1016/j.jcat.2018.03.014.

(10) Ye, J.; Liu, C.; Mei, D.; Ge, Q. Active Oxygen Vacancy Site for Methanol Synthesis from CO_2 Hydrogenation on In_2O_3(110): A DFT Study. *ACS Catal.* **2013**, *3* (6), 1296–1306. https://doi.org/10.1021/cs400132a.

(11) Pinheiro Araújo, T.; Morales-Vidal, J.; Zou, T.; García-Muelas, R.; Willi, P. O.; Engel, K. M.; Safonova, O. V.; Faust Akl, D.; Krumeich, F.; Grass, R. N.; Mondelli, C.; López, N.; Pérez-Ramírez, J. Flame Spray Pyrolysis as a Synthesis Platform to Assess Metal Promotion in In_2O_3-Catalyzed CO_2 Hydrogenation. *Adv. Energy Mater.* **2022**, *12* (14), 2103707. https://doi.org/10.1002/aenm.202103707.

(12) Frei, M. S.; Mondelli, C.; García-Muelas, R.; Kley, K. S.; Puértolas, B.; López, N.; Safonova, O. V.; Stewart, J. A.; Curulla Ferré, D.; Pérez-Ramírez, J. Atomic-Scale Engineering of Indium Oxide Promotion by Palladium for Methanol Production via CO_2 Hydrogenation. *Nat. Commun.* **2019**, *10* (1), 3377. https://doi.org/10.1038/s41467-019-11349-9.

(13) Rui, N.; Wang, Z.; Sun, K.; Ye, J.; Ge, Q.; Liu, C. CO_2 Hydrogenation to Methanol over Pd/In_2O_3: Effects of Pd and Oxygen Vacancy. *Appl. Catal. B Environ.* **2017**, *218*, 488–497. https://doi.org/10.1016/j.apcatb.2017.06.069.

(14) Sun, K.; Rui, N.; Zhang, Z.; Sun, Z.; Ge, Q.; Liu, C.-J. A Highly Active Pt/In_2-O-$_3$ Catalyst for CO_2 Hydrogenation to Methanol with Enhanced Stability. *Green Chem.* **2020**, *22* (15), 5059–5066. https://doi.org/10.1039/D0GC01597K.

(15) Han, Z.; Tang, C.; Wang, J.; Li, L.; Li, C. Atomically Dispersed Ptn+ Species as Highly Active Sites in Pt/In_2O_3 Catalysts for Methanol Synthesis from CO_2 Hydrogenation. *J. Catal.* **2021**, *394*, 236–244. https://doi.org/10.1016/j.jcat.2020.06.018.

(16) Shen, C.; Sun, K.; Zhang, Z.; Rui, N.; Jia, X.; Mei, D.; Liu, C. Highly Active Ir/In2O3 Catalysts for Selective Hydrogenation of CO_2 to Methanol: Experimental and Theoretical Studies. *ACS Catal.* **2021**, *11* (7), 4036–4046. https://doi.org/10.1021/acscatal.0c05628.

(17) Wang, J.; Sun, K.; Jia, X.; Liu, C. CO_2 Hydrogenation to Methanol over Rh/In_2O_3 Catalyst. *Catal. Today* **2021**, *365*, 341–347. https://doi.org/10.1016/j.cattod.2020.05.020.

(18) Wu, Q.; Shen, C.; Rui, N.; Sun, K.; Liu, C. Experimental and Theoretical Studies of CO_2 Hydrogenation to Methanol on Ru/In_2O_3. *J. CO_2 Util.* **2021**, *53*, 101720. https://doi.org/10.1016/j.jcou.2021.101720.

(19) Zhu, J.; Cannizzaro, F.; Liu, L.; Zhang, H.; Kosinov, N.; Filot, Ivo. A. W.; Rabeah, J.; Brückner, A.; Hensen, E. J. M. Ni–In Synergy in CO_2 Hydrogenation to Methanol. *ACS Catal.* **2021**, *11* (18), 11371–11384. https://doi.org/10.1021/acscatal.1c03170.

(20) Jia, X.; Sun, K.; Wang, J.; Shen, C.; Liu, C. Selective Hydrogenation of CO_2 to Methanol over Ni/In_2O_3 Catalyst. *J. Energy Chem.* **2020**, *50*, 409–415. https://doi.org/10.1016/j.jechem.2020.03.083.

(21) Bavykina, A.; Yarulina, I.; Al Abdulghani, A. J.; Gevers, L.; Hedhili, M. N.; Miao, X.; Galilea, A. R.; Pustovarenko, A.; Dikhtiarenko, A.; Cadiau, A.; Aguilar-Tapia, A.; Hazemann, J.-L.; Kozlov, S. M.; Oud-Chikh, S.; Cavallo, L.; Gascon, J. Turning a Methanation Co Catalyst into an In–Co Methanol Producer. *ACS Catal.* **2019**, *9* (8), 6910–6918. https://doi.org/10.1021/acscatal.9b01638.

(22) Sun, K.; Zhang, Z.; Shen, C.; Rui, N.; Liu, C. The Feasibility Study of the Indium Oxide Supported Silver Catalyst for Selective Hydrogenation of CO_2 to Methanol. *Green Energy Environ.* **2022**, *7* (4), 807–817. https://doi.org/10.1016/j.gee.2021.05.004.

(23) Rui, N.; Zhang, F.; Sun, K.; Liu, Z.; Xu, W.; Stavitski, E.; Senanayake, S. D.; Rodriguez, J. A.; Liu, C.-J. Hydrogenation of CO_2 to Methanol on a $Au^{\delta+}$–In_2O_{3-x} Catalyst. *ACS Catal.* **2020**, *10* (19), 11307–11317. https://doi.org/10.1021/acscatal.0c02120.

(24) Rui, N.; Sun, K.; Shen, C.; Liu, C.-J. Density Functional Theoretical Study of Au_4/In_2O_3 Catalyst for CO_2 Hydrogenation to Methanol: The Strong Metal-Support Interaction and Its Effect. *J. CO_2 Util.* **2020**, *42*, 101313. https://doi.org/10.1016/j.jcou.2020.101313.

(25) Wang, X.; Shi, H.; Kwak, J. H.; Szanyi, J. Mechanism of CO_2 Hydrogenation on Pd/Al_2O_3 Catalysts: Kinetics and Transient DRIFTS-MS Studies. *ACS Catal.* **2015**, *5* (11), 6337–6349. https://doi.org/10.1021/acscatal.5b01464.

(26) Matsubu, J.C.; Zhang, S.; DeRita, L.; Marinkovic, N.S.; Chen, J.G.; Graham, G.W,; Pan, X.; Christopher, P. Adsorbate-mediated Strong Metal-Support Interactions in Oxide-Supported Rh Catalysts, *Nature Chem.* **2017**, *9* (4) 120-127 https://doi.org/10.1038/nchem.2607

(27) Lee, W. J.; Li, C.; Prajitno, H.; Yoo, J.; Patel, J.; Yang, Y.; Lim, S. Recent Trend in Thermal Catalytic Low Temperature CO_2 Methanation: A Critical Review. *Catal. Today* **2021**, *368*, 2–19. https://doi.org/10.1016/j.cattod.2020.02.017.

(28) Waluyo, I.; Hunt, A. Ambient Pressure X-Ray Photoelectron Spectroscopy at the IOS (23-ID-2) Beamline at the National Synchrotron Light Source II. *Synchrotron Radiat. News* **2022**, *35* (3), 31–38. https://doi.org/10.1080/08940886.2022.2082180.

(29) Clausen, B. S.; Steffensen, G.; Fabius, B.; Villadsen, J.; Feidenhans'l, R.; Topsøe, H. In Situ Cell for Combined XRD and On-Line Catalysis Tests: Studies of Cu-Based Water Gas Shift and Methanol Catalysts. *J. Catal.* **1991**, *132* (2), 524–535. https://doi.org/10.1016/0021-9517(91)90168-4.

(30) Ravel, B.; Newville, M. ATHENA, ARTEMIS, HEPHAESTUS: Data Analysis for X-Ray Absorption Spectroscopy Using IFEFFIT. *J. Synchrotron Radiat.* **2005**, *12* (4), 537–541. https://doi.org/10.1107/S0909049505012719.

(31) Toby, B. H.; Von Dreele, R. B. *GSAS-II* : The Genesis of a Modern Open-Source All Purpose Crystallography Software Package. *J. Appl. Crystallogr.* **2013**, *46* (2), 544–549. https://doi.org/10.1107/S0021889813003531.

(32) Kresse, G.; Furthmüller, J. Efficiency of Ab-Initio Total Energy Calculations for Metals and Semiconductors Using a Plane-Wave Basis Set. *Comput. Mater. Sci.* **1996**, *6* (1), 15–50. https://doi.org/10.1016/0927-0256(96)00008-0.

(33) Kresse, G.; Hafner, J. Ab Initio Molecular Dynamics for Open-Shell Transition Metals. *Phys. Rev. B* **1993**, *48* (17), 13115–13118. https://doi.org/10.1103/PhysRevB.48.13115.

(34) Kresse, G.; Furthmüller, J. Efficient Iterative Schemes for Ab Initio Total-Energy Calculations Using a Plane-Wave Basis Set. *Phys. Rev. B* **1996**, *54* (16), 11169–11186. https://doi.org/10.1103/PhysRevB.54.11169.

(35) Kresse, G.; Joubert, D. From Ultrasoft Pseudopotentials to the Projector Augmented-Wave Method. *Phys. Rev. B* **1999**, *59* (3), 1758–1775. https://doi.org/10.1103/PhysRevB.59.1758.

(36) Blöchl, P. E. Projector Augmented-Wave Method. *Phys. Rev. B* **1994**, *50* (24), 17953–17979. https://doi.org/10.1103/PhysRevB.50.17953.

(37) Perdew, J. P.; Burke, K.; Ernzerhof, M. Generalized Gradient Approximation Made Simple. *Phys. Rev. Lett.* **1996**, *77* (18), 3865–3868. https://doi.org/10.1103/PhysRevLett.77.3865.

(38) Ye, J.; Liu, C.; Ge, Q. DFT Study of CO_2 Adsorption and Hydrogenation on the In_2O_3 Surface. *J. Phys. Chem. C* **2012**, *116* (14), 7817–7825. https://doi.org/10.1021/jp3004773.

(39) Ye, J.; Liu, C.; Mei, D.; Ge, Q. Methanol Synthesis from CO_2 Hydrogenation over a Pd_4/In_2O_3 Model Catalyst: A Combined DFT and Kinetic Study. *J. Catal.* **2014**, *317*, 44–53. https://doi.org/10.1016/j.jcat.2014.06.002.

(40) Patel, S. K. S.; Dewangan, K.; Srivastav, S. K.; Gajbhiye, N. S. Synthesis of Monodisperse In_2O_3 Nanoparticles and Their D0 Ferromagnetism. *Curr. Appl. Phys.* **2014**, *14* (6), 905–908. https://doi.org/10.1016/j.cap.2014.04.007.

(41) Chen, S.; Abdel-Mageed, A. M.; Dyballa, M.; Parlinska-Wojtan, M.; Bansmann, J.; Pollastri, S.; Olivi, L.; Aquilanti, G.; Behm, R. J. Raising the CO_x Methanation Activity of a $Ru/\gamma\text{-}Al_2O_3$ Catalyst by Activated Modification of Metal–Support Interactions. *Angew. Chem. Int. Ed.* **2020**, *59* (50), 22763–22770. https://doi.org/10.1002/anie.202007228.

(42) Larichev, Y. V.; Moroz, B. L.; Bukhtiyarov, V. I. Electronic State of Ruthenium Deposited onto Oxide Supports: An XPS Study Taking into Account the Final State Effects. *Appl. Surf. Sci.* **2011**, *258* (4), 1541–1550. https://doi.org/10.1016/j.apsusc.2011.09.127.

(43) Martin, R.; Kim, M.; Lee, C. J.; Mehar, V.; Albertin, S.; Hejral, U.; Merte, L. R.; Asthagiri, A.; Weaver, J. F. Isothermal Reduction of $IrO_2(110)$ Films by Methane Investigated Using In Situ X-Ray Photoelectron Spectroscopy. *ACS Catal.* **2021**, *11* (9), 5004–5016. https://doi.org/10.1021/acscatal.1c00702.

(44) Dittmer, J.; Iuzzolino, L.; Dörner, W.; Nolting, H.-F.; Meyer-Klaucke, W.; Dau, H. A New Method for Determination of the Edge Position of X-Ray Absorption Spectra. In *Photosynthesis: Mechanisms and Effects: Volume I–V: Proceedings of the XIth International Congress on Photosynthesis, Budapest, Hungary, August 17–22, 1998*; Garab, G., Ed.; Springer Netherlands: Dordrecht, 1998; pp 1339–1342. https://doi.org/10.1007/978-94-011-3953-3_316.

(45) Powell, C. J. The Quest for Universal Curves to Describe the Surface Sensitivity of Electron Spectroscopies. *J. Electron Spectrosc. Relat. Phenom.* **1988**, *47*, 197–214. https://doi.org/10.1016/0368-2048(88)85012-6.

(46) Insyani, R.; Barus, A. F.; Gunawan, R.; Park, J.; Jaya, G. T.; Cahyadi, H. S.; Sibi, M. G.; Kwak, S. K.; Verma, D.; Kim, J. RuO_2–Ru/Hβ Zeolite Catalyst for High-Yield Direct Conversion of Xylose to Tetrahydrofurfuryl Alcohol. *Appl. Catal. B Environ.* **2021**, *291*, 120120. https://doi.org/10.1016/j.apcatb.2021.120120.

(47) Xin, H.; Lin, L.; Li, R.; Li, D.; Song, T.; Mu, R.; Fu, Q.; Bao, X. Overturning CO_2 Hydrogenation Selectivity with High Activity via Reaction-Induced Strong Metal–Support Interactions. *J. Am. Chem. Soc.* **2022**, *144* (11), 4874–4882. https://doi.org/10.1021/jacs.1c12603.

(48) Tang, H.; Su, Y.; Zhang, B.; Lee, A. F.; Isaacs, M. A.; Wilson, K.; Li, L.; Ren, Y.; Huang, J.; Haruta, M.; Qiao, B.; Liu, X.; Jin, C.; Su, D.; Wang, J.; Zhang, T. Classical Strong Metal–Support Interactions between Gold Nanoparticles and Titanium Dioxide. *Sci. Adv.* **2017**, *3* (10), e1700231. https://doi.org/10.1126/sciadv.1700231.

(49) Zhang, S.; Plessow, P.N.; Willis, J.J.; Sai, S.; Xu, M.; Graham, G.W.; Cargnello, M.; Abild-Pedersen, F.; Pan, X. Dynamical Observation and Detailed Description of Catalysts under Strong Metal-Support Interaction, *Nano Lett.* 2016, 16 (7) 4528-4534, https://doi.org/10.1021/acs.nanolett.6b01769

(50) Wang, C.; Guan, E.; Wang, L.; Chu, X.; Wu, Z.; Zhang, J.; Yang, Z.; Jiang, Y.; Zhang, L.; Meng, X.; Gates, B. C.; Xiao, F.-S. Product Selectivity Controlled by Nanoporous Environments in Zeolite Crystals Enveloping Rhodium Nanoparticle Catalysts for CO_2 Hydrogenation. *J. Am. Chem. Soc.* **2019**, *141* (21), 8482–8488. https://doi.org/10.1021/jacs.9b01555.

(51) Wu, Z.; Saini, N. L.; Agrestini, S.; Castro, D. D.; Bianconi, A.; Marcelli, A.; Battisti, M.; Gozzi, D.; Balducci, G. Ru K-Edge Absorption Study on the $La_{1-x}Ce_xRu$ system. *J. Phys. Condens. Matter* **2000**, *12* (30), 6971–6978. https://doi.org/10.1088/0953-8984/12/30/324.

(52) Liu, Z.; Zhang, F.; Rui, N.; Li, X.; Lin, L.; Betancourt, L. E.; Su, D.; Xu, W.; Cen, J.; Attenkofer, K.; Idriss, H.; Rodriguez, J. A.; Senanayake, S. D. Highly Active Ceria-Supported Ru Catalyst for the Dry Reforming of Methane: In Situ Identification of $Ru^{\delta+}$–Ce^{3+} Interactions for Enhanced Conversion. *ACS Catal.* **2019**, *9* (4), 3349–3359. https://doi.org/10.1021/acscatal.8b05162.

(53) Yevick, A.; Frenkel, A. I. Effects of Surface Disorder on EXAFS Modeling of Metallic Clusters. *Phys. Rev. B* **2010**, *81* (11), 115451. https://doi.org/10.1103/PhysRevB.81.115451.

(54) Tsoukalou, A.; Abdala, P. M.; Stoian, D.; Huang, X.; Willinger, M.-G.; Fedorov, A.; Müller, C. R. Structural Evolution and Dynamics of an In_2O_3 Catalyst for CO_2

Hydrogenation to Methanol: An Operando XAS-XRD and In Situ TEM Study. *J. Am. Chem. Soc.* **2019**, *141* (34), 13497–13505. https://doi.org/10.1021/jacs.9b04873.

(55) Liu, Z.; Huang, E.; Orozco, I.; Liao, W.; Palomino, R. M.; Rui, N.; Duchoň, T.; Nemšák, S.; Grinter, D. C.; Mahapatra, M.; Liu, P.; Rodriguez, J. A.; Senanayake, S. D. Water-Promoted Interfacial Pathways in Methane Oxidation to Methanol on a CeO_2-Cu_2O Catalyst. *Science* **2020**, *368* (6490), 513–517. https://doi.org/10.1126/science.aba5005.

(56) Yang, C.; Pei, C.; Luo, R.; Liu, S.; Wang, Y.; Wang, Z.; Zhao, Z.-J.; Gong, J. Strong Electronic Oxide–Support Interaction over In_2O_3/ZrO_2 for Highly Selective CO_2 Hydrogenation to Methanol. *J. Am. Chem. Soc.* **2020**, *142* (46), 19523–19531. https://doi.org/10.1021/jacs.0c07195.

(57) Palomino, R. M.; Ramírez, P. J.; Liu, Z.; Hamlyn, R.; Waluyo, I.; Mahapatra, M.; Orozco, I.; Hunt, A.; Simonovis, J. P.; Senanayake, S. D.; Rodriguez, J. A. Hydrogenation of CO_2 on ZnO/Cu(100) and ZnO/Cu(111) Catalysts: Role of Copper Structure and Metal–Oxide Interface in Methanol Synthesis. *J. Phys. Chem. B* **2018**, *122* (2), 794–800. https://doi.org/10.1021/acs.jpcb.7b06901.

(58) Wu, Z.; Li, Y.; Huang, W. Size-Dependent Pt-TiO_2 Strong Metal–Support Interaction. *J. Phys. Chem. Lett.* **2020**, *11* (12), 4603–4607. https://doi.org/10.1021/acs.jpclett.0c01560.

(59) Beck, A.; Huang, X.; Artiglia, L.; Zabilskiy, M.; Wang, X.; Rzepka, P.; Palagin, D.; Willinger, M.-G.; van Bokhoven, J. A. The Dynamics of Overlayer Formation on Catalyst Nanoparticles and Strong Metal-Support Interaction. *Nat. Commun.* **2020**, *11* (1), 3220. https://doi.org/10.1038/s41467-020-17070-2.

(60) Tauster, S. J. Strong Metal-Support Interactions. *Acc. Chem. Res.* **1987**, *20* (11), 389–394. https://doi.org/10.1021/ar00143a001.

(61) Campbell, C. T. Electronic Perturbations. *Nat. Chem.* **2012**, *4* (8), 597–598. https://doi.org/10.1038/nchem.1412.

(62) Rodriguez, J. A.; Liu, P.; Graciani, J.; Senanayake, S. D.; Grinter, D. C.; Stacchiola, D.; Hrbek, J.; Fernández-Sanz, J. Inverse Oxide/Metal Catalysts in Fundamental Studies and Practical Applications: A Perspective of Recent Developments. *J. Phys. Chem. Lett.* **2016**, *7* (13), 2627–2639. https://doi.org/10.1021/acs.jpclett.6b00499.

(63) Zhang, J.; Medlin, J. W. Catalyst Design Using an Inverse Strategy: From Mechanistic Studies on Inverted Model Catalysts to Applications of Oxide-Coated Metal

Nanoparticles. *Surf. Sci. Rep.* **2018**, *73* (4), 117–152. https://doi.org/10.1016/j.surfrep.2018.06.002.

(64) Yang, Y.; Mims, C.A.; Mei, D.H.; Peden, C.H.F. Mechanistic Studies of Methanol Synthesis over Cu from $CO/CO_2/H_2/H_2O$ Mixtures: The Source of C in Methanol and the Role of Water, *J. Catal.* **2013**, *298* (1), 10-17. https://doi.org/10.1016/j.jcat.2012.10.028

(65) Graciani, J.; Mudiyanselage, K.; Xu, F.; Baber, A. E.; Evans, J.; Senanayake, S. D.; Stacchiola, D. J.; Liu, P.; Hrbek, J.; Sanz, J. F.; Rodriguez, J. A. Highly Active Copper-Ceria-Titania Catalysts for Methanol Synthesis from CO_2, *Science*, **2014**, *345*, 546– 551, https://doi.org/10.1126/science.1253057

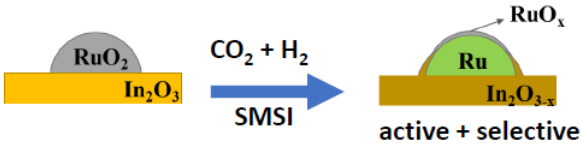

TOC